

Frequency Composition for Compressed and Domain-Adaptive Neural Networks

Yoojin Kwon^{1*} Hongjun Suh^{1*} Wooseok Lee^{1*} Taesik Gong² Songyi Han³ Hyung-Sin Kim¹

¹Seoul National University ²UNIST ³Google

{ideastraw, hjsuh319, andylws, hyungkim}@snu.ac.kr

taesik.gong@unist.ac.kr

syhan@google.com

Abstract

Modern on-device neural network applications must operate under resource constraints while adapting to unpredictable domain shifts. However, this combined challenge—model compression and domain adaptation—remains largely unaddressed, as prior work has tackled each issue in isolation: compressed networks prioritize efficiency within a fixed domain, whereas large, capable models focus on handling domain shifts. In this work, we propose *CoDA*, a frequency composition-based framework that unifies **C**ompression and **D**omain **A**daptation. During training, *CoDA* employs quantization-aware training (QAT) with low-frequency components, enabling a compressed model to selectively learn robust, generalizable features. At test time, it refines the compact model in a source-free manner (i.e., test-time adaptation, TTA), leveraging the full-frequency information from incoming data to adapt to target domains while treating high-frequency components as domain-specific cues. *CoDA* can be integrated synergistically into existing QAT and TTA methods. *CoDA* is evaluated on widely used domain-shift benchmarks, including CIFAR10-C and ImageNet-C, across various model architectures. With significant compression, it achieves accuracy improvements of 7.96%p on CIFAR10-C and 5.37%p on ImageNet-C over the full-precision TTA baseline.

1. Introduction

Resource constraints and domain shifts are critical hurdles for the practical deployment of deep neural networks (DNNs). Research has traditionally tackled these issues in isolation: compressed DNNs focus on efficiency within a fixed target domain (often the same as the source domain) [37, 48], whereas large, capable models handle domain shifts [12, 20, 48]. However, various modern on-device applications, such as extended reality, video surveillance, agricultural monitoring, and autonomous robotics, increasingly demand solutions that handle both [1, 3, 22,

44]. In these scenarios, DNNs must run on resource-constrained devices while simultaneously adapting to dynamic, evolving environments.

In this paper, we investigate **the combined challenges of model compression and domain shifts**, paving the way for robust and efficient DNNs in real-world settings. To achieve this dual goal, we propose *CoDA*, an end-to-end pipeline that spans both training and testing phases to produce compact, robust, and adaptable models. Specifically, we leverage **frequency decomposition** via a 2D Fourier transformation [5], which partitions an image’s spatial characteristics into distinct frequency components [6, 7, 21, 41, 42]. As each frequency component contains non-overlapping information, higher magnitudes in low-frequency components (LFC) suggest that slowly changing patterns, such as smooth textures or surfaces, dominate the image, whereas higher magnitudes in the high-frequency components (HFC) indicate rapidly changing details such as detailed object edges.

During training, *CoDA* aims to create a quantized model that selectively acquires more generalizable knowledge from the source domain. Since a compact model must be highly selective due to limited capacity, we prioritize broader generalization over capturing every fine-grained detail in the source domain. Existing quantization-aware training (QAT) methods, however, do not support this scenario since they focus solely on maximizing source-domain accuracy to match full-precision performance, rather than fostering generalizability [37, 48]. To address this gap, we conduct an empirical study revealing that QAT’s robustness benefits significantly from strategic frequency decomposition (Section 3.2). In particular, training on reconstructed images dominated by LFC enables the quantized model to concentrate on learning generalized features, effectively mitigating its capacity constraints.

After deployment, a compact model that has been robustly trained on LFC may still lack domain-specific details for diverse target domains. On resource-constrained devices in dynamic environments, the model must adapt

*Equal contribution

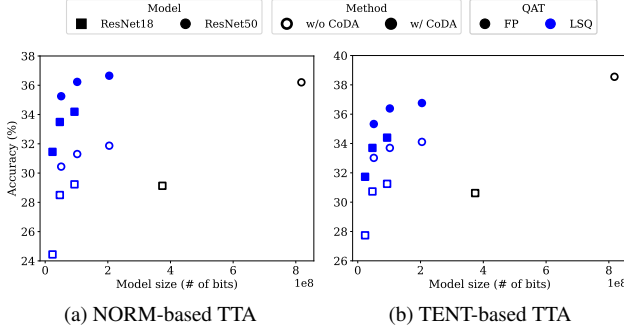


Figure 1. Effectiveness of *CoDA* when applied to various models (ResNet18 and ResNet50), TTA methods (NORM [28, 31] and TENT [34]) and QAT method (LSQ [10]) using three bitwidths (2, 4, and 8 bits). We train on ImageNet and evaluate on ImageNet-C.

to incoming, unlabeled test data in a source-free manner, a process known as test-time adaptation (TTA) [4, 13, 27–29, 31, 34, 47]. To meet this requirement, our test-phase procedure refines the compact model using only target-domain inputs, while preserving the general knowledge acquired during training. Specifically, our TTA utilizes the full-frequency components (FFC) of the test data to capture richer, domain-specific details, treating the LFC (general) and HFC (domain-specific) differently (Section 3.3). This balanced strategy integrates both generalized and domain-specific insights, resulting in a model that is both efficient and robust.

To the best of our knowledge, *CoDA* is the first method to address generalizability and test-time adaptability of *quantized* models. Importantly, rather than competing with existing TTA and QAT methods, *CoDA* can be integrated into these methods. Figure 1 demonstrates *CoDA*’s effectiveness on ResNet-18/50 [15] under domain shifts from ImageNet [9] to ImageNet-C [17]. Notably, when combined with *CoDA*, widely used TTA methods NORM [28, 31] and TENT [34] show significant performance improvements on quantized models. Compared to TTA-applied full-precision models, *CoDA* delivers **up to 5.06%p higher accuracy** on ResNet-18 and achieves comparable performance on ResNet-50, all while **reducing model size by 4-16×**. We further evaluate *CoDA* across various models and domain-shift scenarios, comparing it against existing QAT and TTA methods without using frequency composition. Our results underscore *CoDA*’s ability to simultaneously achieve superior accuracy and significant model compression, highlighting the importance of integrating compression and adaptation for emerging on-device applications.

2. Related Work

2.1. Frequency Decomposition for Computer Vision

Image data can be transformed between the image domain and the frequency domain using 2D discrete cosine trans-

formation or 2D Fourier transformation. The human visual system primarily perceives the LFC of visual data, whereas convolutional neural networks (CNNs) are capable of processing both LFC and HFC [36]. Since labels are generated by humans, who primarily rely on LFC, CNNs can additionally exploit HFC during training. While, HFC are typically learned later than LFC in the training process.

EfficientTrain [39] incorporates this understanding into curriculum learning by initially training with images reconstructed from LFC and gradually transitioning to FFCs in the later stages. Another use of frequency decomposition is domain generalization/adaptation to handle domain shifts. Since each frequency component of images can reserve distinct information, FDA [42] utilizes LFC to create target-style source images. Domain generalization is also explored via middle-frequency components [21] and phase components [7, 41]. Chattopadhyay *et al.* [6] mitigate the lack of HFC in synthetic images for the Syn-to-Real task by adding scaled noise to the amplitude.

2.2. Quantization-Aware Training

Quantization-Aware Training (QAT) aims to optimize both the quantizer and model weights during training. As a result, QAT methods [10, 24, 45, 49] can achieve performance close to that of their full-precision counterparts, unlike post-training quantization (PTQ). LSQ [10] and LQ [45] train uniform and non-uniform quantizers at train time, respectively. However, existing QAT methods have been evaluated only in the source domain, leaving their robustness in dynamic environments largely unexplored. The regularization effect of QAT has been recognized since the first QAT scheme emerged [8], yet little research has focused on this property. Some recent studies have explored the theoretical and domain generalization aspects of QAT models [2, 23, 46]. Our work combines frequency composition with QAT, extending its potential for domain generalization.

2.3. Test-Time Adaptation

Test-Time Adaptation (TTA) aims to adapt a pretrained model to distribution shifts between training and test data in a source-free manner. A common approach involves adjusting batch normalization (BN) layer statistics [27, 28, 31], which include the running means and variances calculated over the entire train data. Nado *et al.* [28] discard the training-based BN statistics and recalculate them based solely on the current test batch. In contrast, Schneider *et al.* [31] and DUA [27] blend training-set statistics with those derived from the test batch. Another line of work adjusts affine parameters in BN layers [13, 14, 29, 30, 34, 38]. Although these methods have shown promise for full-precision models, our work is the first to explore TTA for compact, quantized models.

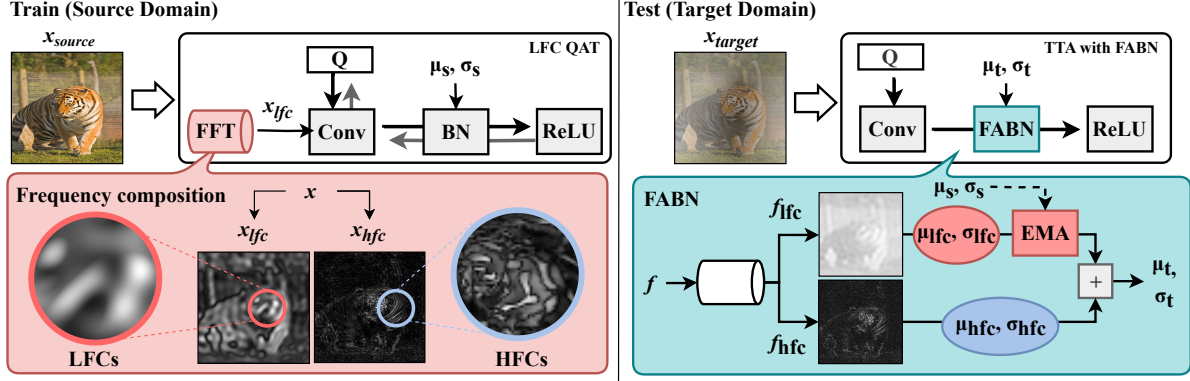


Figure 2. An illustration of the proposed *CoDA*. **Left:** Using Fast Fourier Transformation, an image can be decomposed into HFC consisting of fast-changing patterns (i.e. edges or stripes) and LFC consisting of slow-changing patterns (i.e. smooth shape). During training, *CoDA* focus on learning generalizable features from LFC rather than irregular patterns in HFC (*LFC QAT*). **Right:** At test time, under domain shift, *CoDA* utilizes full-frequency of target data and adapts BN layers with our frequency-aware BN (*FABN*); In the lower frequency of intermediate activations, we utilize running statistics of them to initialize and gradually update the BN statistics. Meanwhile, in the higher frequency, we maintain the original distribution from the activation without composition into source distribution. Finally, both statistics from low-/high-frequency are adequately combined and used to normalize the test batch.

3. Method

We present *CoDA*, an end-to-end pipeline designed to achieve both model compression and test-time adaptation for on-device applications. During training, to handle domain shifts with a low-precision model, we encourage QAT to learning generalizable knowledge from the train data. At test time, TTA should distinguish domain-invariant and domain-specific information in the target data to adapt effectively without discarding general knowledge. To this end, *CoDA* leverages **frequency composition** during both training and test phases.

Our key intuition is that each frequency component in an image, obtained via a Fourier transform, contains distinct information that affects training and testing differently under domain shifts. As shown in Figure 2, dividing an image into LFC and HFC separates smooth and general shapes (LFC) from finer and rapidly changing details (HFC). Therefore, performing QAT on LFC-only data is more robust under domain shifts compared to training on FFCs. At test time, TTA employs FFCs to incorporate the target domain’s specific details, treating information of different frequency range separately. Given that the model learns solely from LFC during training, TTA adapts them to align with the LFC of the target data while simultaneously learning the HFC of the target data from scratch.

Building on these insights, *CoDA* integrates (1) low-frequency components QAT (*LFC QAT*) and (2) TTA with Frequency-aware Batch Normalization (*FABN*), improving both generalizability and adaptability of quantized models.

3.1. Frequency Composition for Input Images

CoDA applies a 2D Fourier transformation $\mathcal{F}(\cdot)$ on an input image \mathbf{x} , converting its spatial pixel patterns into multi-

ple frequency components, $\mathbf{z} = \mathcal{F}(\mathbf{x})$, in the 2D frequency domain. The inverse, $\mathcal{F}^{-1}(\cdot)$, restores spatial information. Given a radius threshold r , low-pass filtering $LPF(\mathbf{z}; r)$ isolates only LFC, while high-pass filtering $HPF(\mathbf{z}; r)$ captures only HFC [36, 39]. The LFC variant \mathbf{x}_{lfc} and HFC variant \mathbf{x}_{hfc} of the original image \mathbf{x} are reconstructed by applying inverse Fourier transformation as follows:

$$\mathbf{x}_{lfc} = \mathcal{F}^{-1}(LPF(\mathbf{z}; r)), \quad \mathbf{x}_{hfc} = \mathcal{F}^{-1}(HPF(\mathbf{z}; r)). \quad (1)$$

Here, \mathbf{x}_{lfc} and \mathbf{x}_{hfc} represent distinct, non-overlapping patterns, so that $\mathbf{x} = \mathbf{x}_{lfc} + \mathbf{x}_{hfc}$. As the radius r increases, LFC data (\mathbf{x}_{lfc}) holds more information, whereas HFC data (\mathbf{x}_{hfc}) contains less. Importantly, as shown in Figure 2, LFC data preserves slowly varying, smooth features, while HFC data retains sharper transitions and intricate details.

3.2. Low-Frequency Components QAT (LFC QAT)

Given that a quantized model has less capacity than its full-precision (FP) counterpart, a QAT scheme requires **strategic and selective learning** to preserve the essential information from the train data. Assuming that LFC information is more generalizable [36, 39, 40, 43] and easier to capture, *CoDA* applies QAT solely to LFC of the train data.

3.2.1. Efficacy of QAT in Learning from LFC

To investigate the effectiveness of LFC QAT, Table 1 compares full-precision (FP) and QAT-applied models (LSQ [10] and LQ [45]) when trained on LFC and HFC that are filtered with various radius. Both LSQ and LQ utilize 2-bit integer quantization for weights and activations (i.e., w2a2), while FP uses 32-bit real values (i.e., w32a32). We use ResNet26 [16] on CIFAR10 [25] and ResNet50 [15] on ImageNet [9], testing all models on FFC data.

Table 1. Classification accuracy(%) of ResNet26 and ResNet50 on CIFAR10 and ImageNet, respectively, with different QAT methods, filter types and radius values for training.

Filter type	CIFAR10 — ResNet26				ImageNet — ResNet50			
	r	FP	LSQ	LQ	r	FP	LSQ	LQ
No filter	-	90.35	86.11	89.06	-	66.96	60.14	63.35
Low pass filter	4	65.66	68.99	71.94	28	59.26	50.61	55.51
	8	81.98	80.82	84.73	56	64.91	58.55	61.83
	12	85.07	83.95	87.48	84	66.24	60.05	62.73
	16	86.83	83.46	88.94	112	66.93	60.51	63.63
High pass filter	4	74.07	54.35	66.45	28	0.17	0.20	0.52
	8	21.21	12.76	19.72	56	0.11	0.13	0.23
	12	11.02	12.00	11.96	84	0.15	0.11	0.22
	16	10.11	10.94	9.63	112	0.15	0.13	0.15

Table 2. Classification accuracy(%) of ResNet26 and ResNet50 on CIFAR10-C and ImageNet-C, respectively, with different QAT methods and various radius values in low pass filters for training.

Filter type	CIFAR10-C — ResNet26				ImageNet-C — ResNet50			
	r	FP	LSQ	LQ	r	FP	LSQ	LQ
No filter	-	53.86	50.15	54.35	-	27.74	19.76	22.44
Low pass filter	4	55.24	59.51	60.60	28	30.40	21.90	25.23
	8	64.61	65.45	67.53	56	29.76	20.82	25.06
	12	63.42	62.24	63.87	84	28.06	19.77	23.20
	16	56.77	55.20	58.10	112	28.08	19.72	23.38

HFC-based Learning. Table 1 shows that all three methods exhibit very low accuracy when trained solely on HFC. In the more challenging ImageNet task, HFC-based training results in $\sim 0\%$ accuracy regardless of the radius r and the method used. This confirms that **LFC contain the necessary information** for image classification. For the easier task of CIFAR10, HFC-based training achieves better accuracy, suggesting the presence of some meaningful information within HFC. For example, with high-pass filtering using a radius of 4, the FP model achieves 74.07% accuracy. However, both LSQ [10] and LQ [45] significantly under-perform compared to the FP model, with an accuracy drop of 8~20%p. This demonstrates the limitations of QAT in effectively learning from HFC compared to FP models.

LFC-based Learning. When trained exclusively on LFC, all three methods maintain decent accuracy on both datasets even as the radius r decreases, confirming the essential role of LFC. Interestingly, on CIFAR10, LQ consistently outperforms the FP models, while LSQ surpasses the FP model when the radius is 4. The superior performance of QAT with a very low precision underscores that **QAT effectively extracts valuable knowledge from LFC**.

3.2.2. Robustness of LFC QAT

Building on the efficacy of QAT with LFC, we further explore the robustness of QAT under domain shifts when exclusively trained on LFC. We evaluate FP (w32a32), LSQ (w2a2), and LQ (w2a2) models, trained on CIFAR10 [25] and ImageNet [9] using LFC with various radius r , by testing on corrupted CIFAR10-C [17] and ImageNet-C [17].

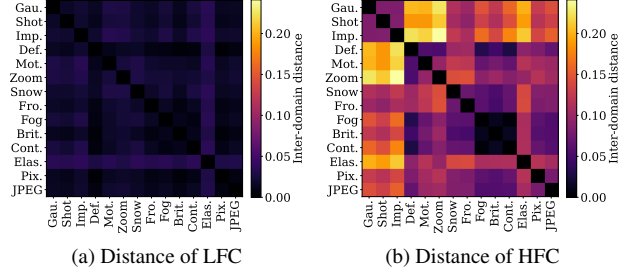


Figure 3. Inter-domain distance matrices of LFC and HFC frequency domain image. The values in Figure 3a appear significantly smaller than those in Figure 3b, indicating that LFC is more domain-invariant compared to HFC. Details of distance matrix calculation are provided in the supplementary materials.

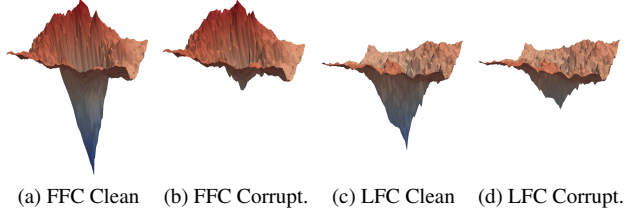


Figure 4. The loss landscapes of quantized ResNet26 on CIFAR10 (Clean) and CIFAR10-C (Corrupt.) trained on different frequency ranges. The quantization method is LSQ [10] and the quantization level is 2-bit. FFC refers to the full frequency of test data; LFC refers to the lower frequency range in a low pass filter of radius 8. Sharpness and concave regions generally indicate less robustness. We use visualization methods following previous works [11, 26].

Table 2 indicates that the robustness of all three methods on ImageNet-C is marginally impacted by the filtering range applied to train data. For example, although LFC with $r=28$ (i.e., the narrowest range) contain much less information than FFC, models trained on these restricted LFC achieve similar or even better accuracy on ImageNet-C compared to those trained on FFC.

Results on CIFAR10-C are more dramatic, with all methods showing significantly enhanced robustness as the filtering range narrows. Specifically, training with LFC at $r=8$ increases accuracy by 11~15%p over FFCs. This demonstrates that the **LFC knowledge remains robust under domain shifts**, whereas HFC information contributes little or can even be detrimental to model robustness. In addition, on CIFAR10-C, LQ (w2a2) provides better accuracy than FP when trained on LFC from CIFAR10. The superior performance of LFC-trained LQ on both CIFAR10 (Table 1) and CIFAR10-C (Table 2) confirms that **QAT effectively learns domain-invariant features from LFC**, resulting in a compressed but generalizable model.

For a deeper understanding, Figure 3 compares the frequency-domain features of LFC and HFC between different corruptions in CIFAR10-C, using 10 random samples per class. The results show that LFC exhibit significantly smaller distances across different corruptions compared to HFC, confirming their domain-invariant properties.

In addition, Figure 4 illustrates the robustness of LFC QAT using the loss landscape visualization [26]. To this end, we train ResNet26 models using the LSQ scheme on either FFC or LFC data in CIFAR10, testing the models on both CIFAR10 (clean) and CIFAR10-C (corrupted). When tested on clean images (Figures 4a and 4c), the FFC-trained model (Figure 4a) achieves a deeper minimum compared to the LFC-trained model (Figure 4c), leading to higher accuracy as shown in Table 2. However, the FFC-trained model has a sharper, partially concave landscape, indicating it may quickly lose its optimal performance under domain shifts.

This vulnerability is confirmed by testing on corrupted images (Figures 4b and 4d), where the FFC-trained model exhibits a deteriorated minimum compared to the LFC-trained model, leading to lower accuracy as shown in Table 2. This shallow landscape suggests that the FFC-trained model must significantly change its parameters (i.e., reshaping the landscape) to handle domain shifts. In contrast, the LFC-trained model presents a smoother, more convex landscape (Figure 4c), indicating a **more malleable state that is well-prepared for future adaptation** under domain shifts.

3.3. TTA with Frequency-Aware BN (FABN)

While LFC QAT shows greater robustness to domain shifts compared to the baseline QATs, further adaption is needed to optimize post-deployment performance on the target data distribution. To achieve this, *CoDA* employs TTA, an emerging paradigm that addresses domain shifts using only unlabeled test samples. Although the model is trained only on LFC, the adaptation phase utilizes FFC data to fully capture domain-specific details comprehensively. However, when adapting batch normalization (BN) statistics for a target domain, existing TTA methods [27, 31] assume that the model has learned from FFC data in the source domain. In contrast, in the context of LFC QAT, the model’s BN statistics contain information of LFC but lack details of HFC from the source domain. This necessitates separately handling LFC and HFC in the target data.

To address this, we propose Frequency-Aware BN (FABN), as in Figure 2. At each time step t , FABN applies two bandpass filters, using the same radius r as the training phase, to separate each BN layer’s input feature \mathbf{f} into low-frequency feature \mathbf{f}_{lfc} and high-frequency feature \mathbf{f}_{hfc} . Then, \mathbf{f}_{lfc} and \mathbf{f}_{hfc} are processed differently as follows:

Adaptation for LFC. For the low-frequency feature \mathbf{f}_{lfc} , we initialize the BN statistics from the source domain as the running mean $\hat{\mu}_{\text{lfc},t}$ and variance $\hat{\sigma}_{\text{lfc},t}$ at test time:

$$\hat{\mu}_{\text{lfc},0} = \hat{\mu}_s, \quad \hat{\sigma}_{\text{lfc},0} = \hat{\sigma}_s, \quad (2)$$

and apply an exponential moving average (EMA) to estimate batch statistics for LFC at time step t as follows:

$$\begin{aligned} \hat{\mu}_{\text{lfc},t} &= (1 - \alpha) \cdot \hat{\mu}_{\text{lfc},t-1} + \alpha \cdot \mu_{\text{lfc},t}, \\ \hat{\sigma}_{\text{lfc},t}^2 &= (1 - \alpha) \cdot \hat{\sigma}_{\text{lfc},t-1}^2 + \alpha \cdot \sigma_{\text{lfc},t}^2. \end{aligned} \quad (3)$$

Table 3. Classification accuracy(%) of *CoDA* on CIFAR10-C. Different frequency range means that test image is filtered through different low-/high-frequency filters before inference and adapted with FABN.

	FFC	LFC			HFC		
		r=4	r=8	r=12	r=4	r=8	r=12
Ours (LSQ w2a2)	71.22	41.94	65.11	66.59	41.78	17.41	10.66
Ours (LQ w2a2)	76.15	42.92	70.11	72.10	45.38	16.67	10.73

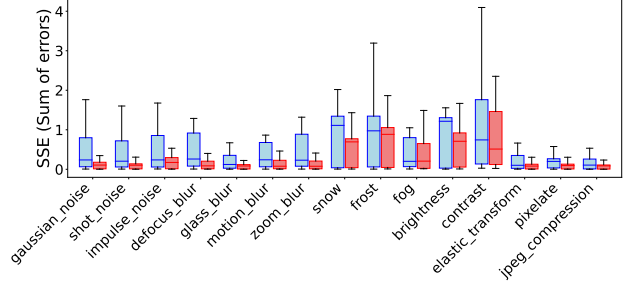


Figure 5. SSE comparison between LSQ [10] with and without *CoDA*. SSE is measured between $\hat{\mu}_s$ and $\hat{\mu}_{\text{lfc},t}$ for the LFC-trained model (*CoDA*), and between $\hat{\mu}_s$ and $\hat{\mu}_t$ for the FFC-trained model. SSE is gathered over all layers. Quantization level is 2-bit.

Here, $\mu_{\text{lfc},t}$ and $\sigma_{\text{lfc},t}^2$ are the mean and variance calculated from the feature \mathbf{f}_{lfc} of the current batch at time t . α is a hyperparameter for EMA.

Adaptation for HFC. Since the model has not learned any high-frequency feature during training, for \mathbf{f}_{hfc} , we do not use the model’s statistics. Instead, we use the mean and variance calculated from the feature \mathbf{f}_{hfc} of the current batch directly as the estimated mean $\hat{\mu}_{\text{hfc},t}$ and variance $\hat{\sigma}_{\text{hfc},t}$ at each time step t :

$$\hat{\mu}_{\text{hfc},t} = \mu_{\text{hfc},t}, \quad \hat{\sigma}_{\text{hfc},t}^2 = \sigma_{\text{hfc},t}^2. \quad (4)$$

Integrating LFC and HFC. After computing the individual mean and standard deviation for \mathbf{f}_{lfc} and \mathbf{f}_{hfc} , we combine them to produce the final BN parameters $\hat{\mu}_t$ and $\hat{\sigma}_t$:

$$\hat{\mu}_t = \hat{\mu}_{\text{lfc},t} + \hat{\mu}_{\text{hfc},t}, \quad \hat{\sigma}_t^2 = \hat{\sigma}_{\text{lfc},t}^2 + \hat{\sigma}_{\text{hfc},t}^2. \quad (5)$$

Importantly, while our FABN adjusts only BN statistics, it can be **synergistically combined** with existing TTA methods that update affine parameters via back propagation, such as TENT [34] and SAR [30].

3.3.1. Impact of Frequency Composition

We conduct an experiment to understand how frequency composition affects the performance of our FABN TTA. For this experiment, CIFAR10 is used for training and CIFAR10-C (severity 5) is used for adaptation and testing. While the model is trained on LFC with $r=8$, various radius of low-/high-frequency filters are applied to test data during adaptation. Table 3 shows the results.

Across all configurations, using FFC rather than LFC or HFC enhances the performance with FABN TTA. This

Table 4. Classification accuracy(%) of ResNet18 and ResNet50 on ImageNet-C with and without TTA. Baseline models are trained with FFCs while ours is trained with LFC. The highest accuracy is in **bold**. In quantized models, both weight and activation values are quantized to 2, 4, and 8 bits.

	ResNet-18								ResNet-50							
	32-bit		2-bit		4-bit		8-bit		32-bit		2-bit		4-bit		8-bit	
	FP	LSQ	LQ	LSQ	LQ	LSQ	LQ	FP	LSQ	LQ	LSQ	LQ	LSQ	LQ	LSQ	LQ
w/o TTA	22.36	16.25	18.66	19.90	20.89	20.15	21.11	27.74	19.76	22.23	21.57	22.96	22.58	15.70		
NORM [28]	29.13	24.44	28.35	28.50	28.68	29.23	30.42	36.20	30.44	32.65	31.30	31.93	31.87	26.52		
CoDA	-	31.45	34.28	33.49	34.47	34.19	34.50	-	35.25	38.03	36.23	36.47	36.65	35.21		
TENT [34]	30.62	27.74	30.42	30.73	30.07	31.25	31.71	38.55	33.02	35.03	33.70	33.96	34.11	30.96		
TENT + CoDA	-	31.73	34.29	33.70	33.83	34.40	34.47	-	35.33	37.99	36.39	33.83	36.76	35.21		
SAR [30]	33.88	29.47	30.42	31.86	30.07	32.13	31.70	41.49	34.02	35.04	34.40	33.95	34.86	30.95		
SAR + CoDA	-	31.22	34.17	33.56	33.71	34.41	34.35	-	35.78	37.90	36.49	36.40	36.73	35.09		

demonstrates the importance of using full-frequency during the adaptation stage, even though the model is trained only on LFC. Specifically, Table 3 shows that unlike the efficacy achieved from LFC-based training, a smaller range of LFC degrades adaptation performance compared to FFC adaptation. When the radius r for test data is 4, smaller than that for the training data (i.e., $r=8$), the model performance is even degraded after adaptation. Similarly, relying only on HFC often fails at adaptation. Overall, **both LFC and HFC significantly contribute to FABN TTA** by providing rich information in the target domain.

3.3.2. Interaction with LFC QAT

The rationale for integrating LFC QAT and FABN is that a model trained with LFC QAT, being inherently more robust than one trained with FFC QAT, may require only modest adaptation of its BN parameters for LFC data at test time. To investigate this, Figure 5 depicts the sum of squared errors (SSE) between $\hat{\mu}_s$ and $\hat{\mu}_{lfc,t}$ in the LFC-trained model, and between $\hat{\mu}_s$ and $\hat{\mu}_t$ in the FFC-trained model under various domain shifts. In all configurations, the LFC BN parameters of the LFC-trained model demonstrate a lower need for adaptation than the full BN parameters of the FFC-trained model. This suggests that LFC BN parameters are more stable under domain shifts, supporting the approach of treating them separately from HFC BN parameters.

4. Evaluation

Datasets. We use four widely recognized benchmarks for evaluating model robustness under domain shifts. CIFAR10-C [17] is used as target data for models trained on CIFAR10 [25], while ImageNet-C [17], ImageNet-R [18], and ImageNet-Sketch [35] serve as target data for models trained on ImageNet.

Network architectures. We evaluate various models including the ResNet [16], MobileNet [19] and EfficientNet [32] architectures to compare the size and performance of different models.

QAT & TTA Methods. Two general QAT methods are used for this study: LSQ [10] and LQ [45]. Four other TTA methods are used in comparison to CoDA: NORM [28, 31], TENT [34], SAR [30], and CoTTA [38]. Further implementation details are described in supplementary materials.

4.1. Overall Results

Tables 4, 5, and 6 show TTA performance on ImageNet-C, CIFAR10-C, and ImageNet-R/-Sketch dataset, respectively. While ImageNet-C and CIFAR10-C are standard TTA benchmarks, ImageNet-R/-Sketch are additionally utilized for evaluating generalizability of our approach.

ImageNet-C. Table 4 shows that all TTA baselines [28, 30, 34] suffer performance degradation when adapting FFC-trained quantized models. Compared to the TTA accuracy of their full-precision (FP) counterparts, these baselines generally struggle with reduced precision. In contrast, CoDA integrates seamlessly with various TTA and QAT baselines, boosting performance across different architectures and bitwidth settings. In all settings, CoDA-enhanced methods achieve state-of-the-art results. Notably, on ResNet-18, CoDA even outperforms full-precision models with TTA by **up to 5.37%p**, while **reducing model size by 4 to 16 times**. These results demonstrate that CoDA’s end-to-end pipeline, combining LFC-based QAT and frequency-decomposed TTA, effectively tackles both model compression and domain shifts.

CIFAR10-C. Table 5 shows that CoDA on both LQ and LSQ outperforms the TTA baselines in all bitwidths. CoDA shows better performance compared to FP models that are larger in capacity, showing consistency with ImageNet-C experiment results. Specifically, CoDA demonstrates **up to 7.96%p higher accuracy** compared to TTA-applied FP models while reducing model size by **4 to 16 times**, proving the effectiveness of our approach.

ImageNet-R/-Sketch. Table 6 shows that CoDA remains effective on domain shift datasets other than corruption, mostly outperforming other TTA baselines.

Table 5. Classification accuracy(%) of ResNet26 on CIFAR10-C with and without TTA. Baseline models are trained with FFC while ours is trained with LFC. The highest accuracy is in **bold**.

Method	32-bit	2bit		4bit		8bit	
	FP	LSQ	LQ	LSQ	LQ	LSQ	LQ
w/o TTA	58.43	58.86	59.72	52.65	55.40	51.60	53.16
NORM	68.42	65.52	69.29	64.23	68.05	64.23	67.47
TENT	72.64	70.18	73.72	70.43	73.15	71.09	72.90
SAR	71.66	68.99	73.60	69.46	73.16	69.52	73.06
<i>CoDA</i>	-	71.22	76.15	72.50	76.38	72.86	75.52

Table 6. Classification accuracy(%) of ResNet18/50 on ImageNet-R/-Sketch with and without TTA. Baseline models are trained with FFCs while ours is trained with LFCs. Both weight and activation values are quantized to 2 bits. The highest accuracy is in **bold**.

	ImageNet-R				ImageNet-Sketch			
	ResNet-18		ResNet-50		ResNet-18		ResNet-50	
	LSQ	LQ	LSQ	LQ	LSQ	LQ	LSQ	LQ
w/o TTA	19.64	21.96	21.77	24.93	9.62	11.51	10.62	13.58
NORM [28]	21.66	24.22	23.65	27.16	11.38	12.87	12.58	16.02
TENT [34]	20.54	23.59	23.29	26.79	10.15	11.65	12.71	15.33
SAR [30]	20.87	23.56	23.26	26.70	10.82	11.69	12.99	15.28
<i>CoDA</i>	21.85	24.58	24.02	27.81	9.90	12.98	13.30	16.21

Table 7. Classification accuracy (%) of different lightweight models on CIFAR10-C when LSQ is used for the QAT method. The highest accuracy is in **bold**.

	32-bit	2-bit	4-bit	8-bit
MobileNet v3-small				
w/o TTA	54.74	53.38	55.46	53.89
NORM [28]	68.85	69.71	70.01	69.11
TENT [34]	73.83	74.38	75.23	74.90
SAR [30]	73.82	74.33	75.09	74.85
<i>CoDA</i>	-	74.49	75.92	75.71
MobileNet v3-large				
w/o TTA	58.11	56.55	55.41	56.71
NORM [28]	72.34	72.86	72.96	73.27
TENT [34]	77.26	76.76	77.57	77.32
SAR [30]	77.05	76.72	77.51	77.32
<i>CoDA</i>	-	77.51	79.40	80.06
EfficientNet-b0				
w/o TTA	57.41	54.85	60.25	59.52
NORM [28]	70.60	71.75	74.01	73.93
TENT [34]	79.04	78.42	79.03	79.18
SAR [30]	78.89	78.20	78.69	79.00
<i>CoDA</i>	-	78.59	80.41	80.62

In summary, our evaluation on benchmarks against existing methods highlights the practical advantages of intelligently leveraging frequency components, especially in scenarios where domain shifts and limited resources co-exist. *CoDA* maintains robust performance across diverse operational settings, making it a compelling solution for real-world applications with varying data distributions.

Table 8. Classification accuracy(%) of ResNet18 on ImageNet-C under continually changing target domain with TTA. The model parameters never be reset except for the case of stochastic restoration by CoTTA. Baseline models are trained with FFC while ours is trained with LFC. The highest accuracy is in **bold**.

	FP	LSQ		
	32-bit	2-bit	4-bit	8-bit
w/o TTA	22.36	16.25	19.90	20.15
TENT [34]	32.76	28.70	31.63	32.06
CoTTA [38]	34.14	17.72	31.87	32.44
<i>CoDA</i>	-	31.35	33.43	34.07

Table 9. Classification accuracy (%) by varying ablative settings in *CoDA* on CIFAR10-C and ImageNet-C. ‘‘Base’’ refers to FFC-based learning on QAT. The highest accuracy is in **bold**.

	LFC	FABN	CIFAR10-C	ImageNet-C
Base			59.72	22.23
LFC-only	✓		67.58	23.44
FABN-only		✓	73.96	35.98
LFC + FABN (<i>CoDA</i>)	✓	✓	76.15	38.03

4.2. Lightweight Models

We conduct extensive experiments on more lightweight model architectures such as MobileNet [19] and EfficientNet [32] which are designed to efficiently learn visual information with a minimum amount of parameters. Table 7 shows that *CoDA* is still effective beyond the baseline TTAs under quantization. *CoDA* achieves the highest top-1 accuracy across all models, even surpassing FP models, demonstrating that selective learning on domain-agnostic LFC information and frequency-based TTA enhance robustness, even in the lightweight models.

4.3. Continual Domain Shifts

We also investigate robustness under continually changing target domains, comparing *CoDA* with CoTTA [38], which is designed to alleviate catastrophic forgetting. As shown in Table 8, while *CoDA* is not specifically designed to address the forgetting issue, it achieves competitive or even higher accuracy than CoTTA [38]. This is because *CoDA* retains only domain-agnostic LFC information and entirely changes domain-specific HFC information in BN statistics across changing domains.

4.4. Ablation Study

Impact of individual components. We conduct an ablative study to further investigate the effectiveness of *CoDA*’s technical components: Low-Frequency QAT (LFC) and Frequency-Aware BN (FABN). Table 9 shows the result for CIFAR10-C with ResNet26 and ImageNet-C with ResNet50 with 2-bit quantized LQ [45]. ‘Base’ refers to FFC-based learning on QAT. Each component shows improvement over Base. Notably, on ImageNet-C, the accu-

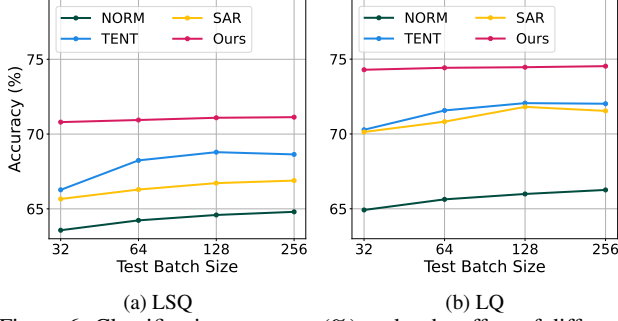


Figure 6. Classification accuracy (%) under the effect of different batch sizes and TTA methods on CIFAR10-C with ResNet26.

racy gap (15.8%p) between *CoDA* and Base has a larger improvement over the sum of the individual gains of LFC-only (1.21%p) and FABN-only (12.54%p). This highlights the synergy between LFC and FABN within *CoDA*.

Impact of test batch size. We also investigate the effect of varying test batch size, which impacts the adaptation process of BN-based TTA methods. Figure 6 shows the result on CIFAR10-C. We found that the performance of NORM, TENT, and SAR drops significantly when the batch size is smaller, indicating that they are susceptible to smaller batch sizes. In contrast, *CoDA* shows robustness over various batch sizes. This is mainly because it retains the well-trained LFC running mean, while rapidly adapting to the HFC of each incoming batch.

4.5. Feature Embedding Analysis

To further understand the compatibility between QAT and LFC (Section 3.2), we visualize feature embeddings of three example classes (airplane, automobile, and bird) in CIFAR10 using t-SNE [33] (Figure 7). We train ResNet26 with full precision and using LSQ and LQ schemes on either FFC or LFC data in CIFAR10, testing the models on both CIFAR10 (clean) and CIFAR10-C (corrupted).

For all cases including FP, LSQ, and LQ, the LFC-trained models achieve significantly better feature alignment between clean (solid circles) and corrupted (empty circles) images within each class. Interestingly, when trained on FFC information, both LSQ and LQ exhibit more dispersed feature embeddings across multiple clusters compared to FP, demonstrating QAT’s weakness in learning generalizable information from the source domain. However, this limitation is alleviated when using only LFCs during training. In the LFC-trained models, both LSQ and LQ enable feature embeddings to converge around a primary cluster. For instance, the bird class (green) is dispersed in the FFC-trained models but forms a more cohesive cluster in the LFC-trained models. Overall, the results show empirical evidence of the compatibility between QAT and LFC, suggesting that LFC-based QAT is promising for addressing resource constraints and domain shifts simultaneously.

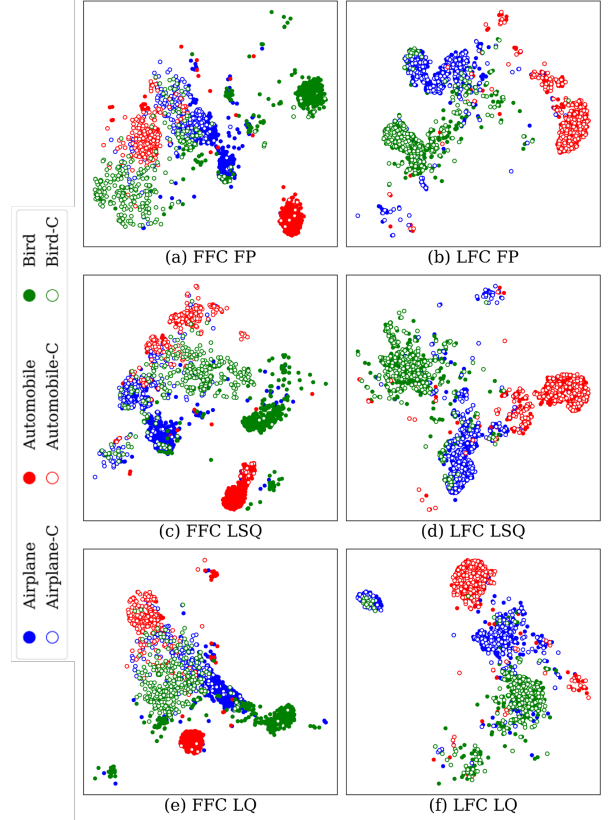


Figure 7. t-SNE visualization of embeddings from FFC/LFC-trained FP, LSQ [10], and LQ [45] models. Tested on three example classes (airplane, automobile, and bird) of CIFAR10-C with pixelate corruption (severity 5). Overlapping embeddings of clean and corrupted images in LFC indicate natural feature alignment.

5. Conclusion

This study highlights the necessity of tackling compression and adaptation jointly when deploying neural networks on resource-constrained devices in dynamic environments—an area previously overlooked by standard QAT and TTA baselines. To address this gap, we introduced *CoDA*, a novel frequency-aware framework that unifies QAT and TTA by leveraging LFCs at training time and FABN at test time. This combination enhances both the robustness and adaptability of quantized models under domain shifts. Our main results demonstrate substantial accuracy gains in low-bit settings, underscoring the efficacy of *CoDA* for practical deployment. Furthermore, our extensive evaluations with various models and datasets show that *CoDA* effectively retains LFC even in lightweight models and applies to diverse distributions and datasets. Our findings reveal the positive impact of selectively and adaptively exploiting frequency components for both training and adaptation. We believe this opens a promising path toward more effective, domain-resilient neural network deployment in real-world applications.

References

- [1] Michele Antonazzi, Matteo Luperto, N Alberto Borghese, and Nicola Basilico. R2snet: Scalable domain adaptation for object detection in cloud-based robotic ecosystems via proposal refinement. In *2024 IEEE/RSJ International Conference on Intelligent Robots and Systems (IROS)*, pages 2676–2682. IEEE, 2024. 1
- [2] MohammadHossein AskariHemmat, Ahmadreza Jeddi, Reyhane Askari Hemmat, Ivan Lazarevich, Alexander Hoffman, Sudhakar Sah, Ehsan Saboori, Yvon Savaria, and Jean-Pierre David. Qgen: On the ability to generalize in quantization aware training. *arXiv preprint arXiv:2404.11769*, 2024. 2
- [3] Michele Boldo, Mirco De Marchi, Enrico Martini, Stefano Aldegheri, and Nicola Bombieri. Domain-adaptive online active learning for real-time intelligent video analytics on edge devices. *IEEE Transactions on Computer-Aided Design of Integrated Circuits and Systems*, 43(11):4105–4116, 2024. 1
- [4] Malik Boudiaf, Romain Mueller, Ismail Ben Ayed, and Luca Bertinetto. Parameter-free online test-time adaptation. In *Proceedings of the IEEE/CVF Conference on Computer Vision and Pattern Recognition*, pages 8344–8353, 2022. 2
- [5] E Oran Brigham. *The fast Fourier transform and its applications*. Prentice-Hall, Inc., 1988. 1
- [6] Prithvijit Chattopadhyay, Kartik Sarangmath, Vivek Vijaykumar, and Judy Hoffman. Pasta: Proportional amplitude spectrum training augmentation for syn-to-real domain generalization. In *Proceedings of the IEEE/CVF International Conference on Computer Vision*, pages 19288–19300, 2023. 1, 2
- [7] Guangyao Chen, Peixi Peng, Li Ma, Jia Li, Lin Du, and Yonghong Tian. Amplitude-phase recombination: Rethinking robustness of convolutional neural networks in frequency domain. In *Proceedings of the IEEE/CVF International Conference on Computer Vision*, pages 458–467, 2021. 1, 2
- [8] Matthieu Courbariaux, Yoshua Bengio, and Jean-Pierre David. Binaryconnect: Training deep neural networks with binary weights during propagations. *Advances in neural information processing systems*, 28, 2015. 2
- [9] Jia Deng, Wei Dong, Richard Socher, Li-Jia Li, Kai Li, and Li Fei-Fei. Imagenet: A large-scale hierarchical image database. In *2009 IEEE conference on computer vision and pattern recognition*, pages 248–255. Ieee, 2009. 2, 3, 4, 12
- [10] Steven K Esser, Jeffrey L McKinstry, Deepika Bablani, Rathinakumar Appuswamy, and Dharmendra S Modha. Learned step size quantization. *arXiv preprint arXiv:1902.08153*, 2019. 2, 3, 4, 5, 6, 8, 12
- [11] Pierre Foret, Ariel Kleiner, Hossein Mobahi, and Behnam Neyshabur. Sharpness-aware minimization for efficiently improving generalization. *arXiv preprint arXiv:2010.01412*, 2020. 4, 13
- [12] Amir Gholami, Sehoon Kim, Zhen Dong, Zhewei Yao, Michael W Mahoney, and Kurt Keutzer. A survey of quantization methods for efficient neural network inference. In *Low-Power Computer Vision*, pages 291–326. Chapman and Hall/CRC, 2022. 1
- [13] Taesik Gong, Jongheon Jeong, Taewon Kim, Yewon Kim, Jinwoo Shin, and Sung-Ju Lee. Note: Robust continual test-time adaptation against temporal correlation. *Advances in Neural Information Processing Systems*, 35:27253–27266, 2022. 2
- [14] Taesik Gong, Yewon Kim, Taeckyoung Lee, Sorn Chotananurak, and Sung-Ju Lee. Sotta: Robust test-time adaptation on noisy data streams. *Advances in Neural Information Processing Systems*, 36, 2024. 2
- [15] Kaiming He, Xiangyu Zhang, Shaoqing Ren, and Jian Sun. Deep residual learning for image recognition. In *Proceedings of the IEEE conference on computer vision and pattern recognition*, pages 770–778, 2016. 2, 3, 12
- [16] Kaiming He, Xiangyu Zhang, Shaoqing Ren, and Jian Sun. Identity mappings in deep residual networks. In *Computer Vision—ECCV 2016: 14th European Conference, Amsterdam, The Netherlands, October 11–14, 2016, Proceedings, Part IV 14*, pages 630–645. Springer, 2016. 3, 6, 12
- [17] Dan Hendrycks and Thomas Dietterich. Benchmarking neural network robustness to common corruptions and perturbations. *arXiv preprint arXiv:1903.12261*, 2019. 2, 4, 6, 12
- [18] Dan Hendrycks, Steven Basart, Norman Mu, Saurav Kadavath, Frank Wang, Evan Dorundo, Rahul Desai, Tyler Zhu, Samyak Parajuli, Mike Guo, et al. The many faces of robustness: A critical analysis of out-of-distribution generalization. In *Proceedings of the IEEE/CVF international conference on computer vision*, pages 8340–8349, 2021. 6, 12
- [19] Andrew Howard, Mark Sandler, Grace Chu, Liang-Chieh Chen, Bo Chen, Mingxing Tan, Weijun Wang, Yukun Zhu, Ruoming Pang, Vijay Vasudevan, et al. Searching for mobilenetv3. In *Proceedings of the IEEE/CVF international conference on computer vision*, pages 1314–1324, 2019. 6, 7
- [20] Lukas Hoyer, Dengxin Dai, and Luc Van Gool. Daformer: Improving network architectures and training strategies for domain-adaptive semantic segmentation. In *Proceedings of the IEEE/CVF Conference on Computer Vision and Pattern Recognition*, pages 9924–9935, 2022. 1

- [21] Jiaxing Huang, Dayan Guan, Aoran Xiao, and Shijian Lu. Fsd: Frequency space domain randomization for domain generalization. In *Proceedings of the IEEE/CVF Conference on Computer Vision and Pattern Recognition*, pages 6891–6902, 2021. 1, 2
- [22] Raza Imam, Muhammad Huzaifa, Nabil Mansour, Shaher Bano Mirza, and Fouad Lamghari. Domain adaptable fine-tune distillation framework for advancing farm surveillance. *arXiv preprint arXiv:2402.07059*, 2024. 1
- [23] Saqib Javed, Hieu Le, and Mathieu Salzmann. Qt-dog: Quantization-aware training for domain generalization. *arXiv preprint arXiv:2410.06020*, 2024. 2
- [24] Qing Jin, Linjie Yang, Zhenyu Liao, and Xiaoning Qian. Neural network quantization with scale-adjusted training. In *BMVC*, 2020. 2
- [25] Alex Krizhevsky, Geoffrey Hinton, et al. Learning multiple layers of features from tiny images. 2009. 3, 4, 6, 12
- [26] Hao Li, Zheng Xu, Gavin Taylor, Christoph Studer, and Tom Goldstein. Visualizing the loss landscape of neural nets. *Advances in neural information processing systems*, 31, 2018. 4, 5, 13
- [27] M Jehanzeb Mirza, Jakub Micorek, Horst Possegger, and Horst Bischof. The norm must go on: Dynamic unsupervised domain adaptation by normalization. In *Proceedings of the IEEE/CVF conference on computer vision and pattern recognition*, pages 14765–14775, 2022. 2, 5
- [28] Zachary Nado, Shreyas Padhy, D Sculley, Alexander D’Amour, Balaji Lakshminarayanan, and Jasper Snoek. Evaluating prediction-time batch normalization for robustness under covariate shift. *arXiv preprint arXiv:2006.10963*, 2020. 2, 6, 7, 13
- [29] Shuaicheng Niu, Jiayang Wu, Yifan Zhang, Yaofo Chen, Shijian Zheng, Peilin Zhao, and Mingkui Tan. Efficient test-time model adaptation without forgetting. In *International conference on machine learning*, pages 16888–16905. PMLR, 2022. 2
- [30] Shuaicheng Niu, Jiayang Wu, Yifan Zhang, Zhiquan Wen, Yaofo Chen, Peilin Zhao, and Mingkui Tan. Towards stable test-time adaptation in dynamic wild world. *arXiv preprint arXiv:2302.12400*, 2023. 2, 5, 6, 7, 13
- [31] Steffen Schneider, Evgenia Rusak, Luisa Eck, Oliver Bringmann, Wieland Brendel, and Matthias Bethge. Improving robustness against common corruptions by covariate shift adaptation. *Advances in neural information processing systems*, 33:11539–11551, 2020. 2, 5, 6, 13
- [32] Mingxing Tan and Quoc Le. Efficientnet: Rethinking model scaling for convolutional neural networks. In *International conference on machine learning*, pages 6105–6114. PMLR, 2019. 6, 7
- [33] Laurens Van der Maaten and Geoffrey Hinton. Visualizing data using t-sne. *Journal of machine learning research*, 9(11), 2008. 8
- [34] Dequan Wang, Evan Shelhamer, Shaoteng Liu, Bruno Olshausen, and Trevor Darrell. Tent: Fully test-time adaptation by entropy minimization. *arXiv preprint arXiv:2006.10726*, 2020. 2, 5, 6, 7, 13
- [35] Haohan Wang, Songwei Ge, Zachary Lipton, and Eric P Xing. Learning robust global representations by penalizing local predictive power. *Advances in neural information processing systems*, 32, 2019. 6, 12
- [36] Haohan Wang, Xindi Wu, Zeyi Huang, and Eric P Xing. High-frequency component helps explain the generalization of convolutional neural networks. In *Proceedings of the IEEE/CVF conference on computer vision and pattern recognition*, pages 8684–8694, 2020. 2, 3
- [37] Jindong Wang, Cuiling Lan, Chang Liu, Yidong Ouyang, Tao Qin, Wang Lu, Yiqiang Chen, Wenjun Zeng, and S Yu Philip. Generalizing to unseen domains: A survey on domain generalization. *IEEE transactions on knowledge and data engineering*, 35 (8):8052–8072, 2022. 1
- [38] Qin Wang, Olga Fink, Luc Van Gool, and Dengxin Dai. Continual test-time domain adaptation. In *Proceedings of the IEEE/CVF Conference on Computer Vision and Pattern Recognition*, pages 7201–7211, 2022. 2, 6, 7, 13
- [39] Yulin Wang, Yang Yue, Rui Lu, Tianjiao Liu, Zhao Zhong, Shiji Song, and Gao Huang. Efficienttrain: Exploring generalized curriculum learning for training visual backbones. In *Proceedings of the IEEE/CVF International Conference on Computer Vision*, pages 5852–5864, 2023. 2, 3
- [40] Kai Xu, Minghai Qin, Fei Sun, Yuhao Wang, Yen-Kuang Chen, and Fengbo Ren. Learning in the frequency domain. In *Proceedings of the IEEE/CVF conference on computer vision and pattern recognition*, pages 1740–1749, 2020. 3
- [41] Qinwei Xu, Ruipeng Zhang, Ya Zhang, Yanfeng Wang, and Qi Tian. A fourier-based framework for domain generalization. In *Proceedings of the IEEE/CVF conference on computer vision and pattern recognition*, pages 14383–14392, 2021. 1, 2
- [42] Yanchao Yang and Stefano Soatto. Fda: Fourier domain adaptation for semantic segmentation. In *Proceedings of the IEEE/CVF conference on computer vision and pattern recognition*, pages 4085–4095, 2020. 1, 2
- [43] Dong Yin, Raphael Gontijo Lopes, Jon Shlens, Ekin Dogus Cubuk, and Justin Gilmer. A fourier per-

- spective on model robustness in computer vision. *Advances in Neural Information Processing Systems*, 32, 2019. [3](#)
- [44] Xiangyun Zeng, Siok Yee Tan, and Mohammad Faizul Nasrudin. Adapt-net: A unified object detection framework for mobile augmented reality. *IEEE Access*, 2024. [1](#)
 - [45] Dongqing Zhang, Jiaolong Yang, Dongqiangzi Ye, and Gang Hua. Lq-nets: Learned quantization for highly accurate and compact deep neural networks. In *Proceedings of the European conference on computer vision (ECCV)*, pages 365–382, 2018. [2](#), [3](#), [4](#), [6](#), [7](#), [8](#)
 - [46] Kaiqi Zhang, Ming Yin, and Yu-Xiang Wang. Why quantization improves generalization: Ntk of binary weight neural networks. *arXiv preprint arXiv:2206.05916*, 2022. [2](#)
 - [47] Marvin Zhang, Sergey Levine, and Chelsea Finn. Memo: Test time robustness via adaptation and augmentation. *Advances in neural information processing systems*, 35:38629–38642, 2022. [2](#)
 - [48] Sicheng Zhao, Xiangyu Yue, Shanghang Zhang, Bo Li, Han Zhao, Bichen Wu, Ravi Krishna, Joseph E Gonzalez, Alberto L Sangiovanni-Vincentelli, Sanjit A Seshia, et al. A review of single-source deep unsupervised visual domain adaptation. *IEEE Transactions on Neural Networks and Learning Systems*, 33(2):473–493, 2020. [1](#)
 - [49] Shuchang Zhou, Yuxin Wu, Zekun Ni, Xinyu Zhou, He Wen, and Yuheng Zou. Dorefa-net: Training low bitwidth convolutional neural networks with low bitwidth gradients. *arXiv preprint arXiv:1606.06160*, 2016. [2](#)

Frequency Composition for Compressed and Domain-Adaptive Neural Networks

(Supplementary Material)

A. Experimental Details

We use pre-activation [16] based ResNet [15] models. All models are trained from scratch. ResNet26 [16] is used for training on CIFAR10 [25], while ResNet18/50 [15] are used for training on ImageNet [9]. In frequency analysis (Section 3), we use three different random seeds to train and test on CIFAR10 [25] / CIFAR10-C [17], reporting the average accuracies and standard deviations. For ImageNet [9], only one random seed is used due to the significant computational burden caused by its sheer volume. For CIFAR10 [25], we run our training on a single GPU (NVIDIA GeForce RTX 3090) and 4 multi GPUs (NVIDIA GeForce A100) for ImageNet [9].

A.1. Datasets Details

CIFAR10 / CIFAR10-C. CIFAR10 [25] consists of 60,000 images of size 32×32 pixels across 10 classes, with 6,000 images per class. It is divided into 50,000 training images and 10,000 test images. CIFAR10-C [17] applies 15 types of corruption which includes noise, blur, weather effects, and digital distortions, to CIFAR10 test data. Each corruption type includes a total of 50,000 for 5 severity levels - 10,000 per each level.

ImageNet / ImageNet-C. ImageNet [9] consists of 1,331,167 images of varying image sizes across 1,000 classes. It is divided into 1,281,167 training images and 50,000 validation images. Throughout the whole paper, the test set of ImageNet refers to the validation set of ImageNet. ImageNet-C [17] applies 15 types of corruption to ImageNet test data, equivalent to CIFAR10-C. Each corruption type includes a total of 250,000 for 5 severity levels - 50,000 per each level.

ImageNet-R / ImageNet-Sketch. ImageNet-R [18] consists of 30,000 images, containing various naturally occurring renditions (e.g., painting, sculpture, embroidery, etc.) of 200 ImageNet object classes. ImageNet-Sketch [35] consists of 50,000 images, containing 50 sketch images for each of the 1000 ImageNet classes.

A.2. Baseline Details

For baselines, we refer to the official implementations of the original authors. We use the hyperparameters reported on their paper and code. We use torch.optim.SGD for training.

Also, we utilize 2-bit quantized models for LSQ and LQ, unless specified otherwise. For experiments in model comparison (Figure 1), LSQ 4-/8-bits quantized ResNet18/50 are also used. Additional details of the implementations are provided below.

A.2.1. FP

FP. Full-precision models are not quantized.

For CIFAR10, we use learning rate (lr) as 0.1, momentum as 0.9, and weight decay as 1.0e-4. The learning rate scheduler is set to torch.optim.lr_scheduler.StepLR with step size 30. Batch size is 32 and each model is trained for 90 epochs.

For ImageNet, we use learning rate (lr) as 0.1, momentum as 0.9, and weight decay as 1.0e-4. Learning rate scheduler is set to torch.optim.lr_scheduler.StepLR with step size 30. Batch size is 256 and each model is trained for 90 epochs.

A.2.2. QAT

LSQ. Following the original paper, [10], we initialize step size s as $s=2\overline{w}p$ where \overline{w} refers to the mean of weights in the corresponding layer and p is $2^{\text{bitwidth}-1} - 1$. We use the reported hyperparameter setting which showed the best accuracy by each hyperparameter.

For CIFAR10, we use learning rate (lr) as 0.1, momentum as 0.9, and weight decay as 5.0e-4. Learning rate scheduler (lrsch) is set to MultiStepLR of torch.optim.lr_scheduler with milestones of [10, 30, 50, 70]. Batch size is 256 and each model is trained for 90 epochs.

For ImageNet, we use learning rate (lr) as 0.01, momentum as 0.9, and weight decay as 2.5e-4. Learning rate scheduler (lrsch) is set to CosineAnnealingLR of torch.optim.lr_scheduler with Tmax is 90. Batch size is 256 and each model is trained for 90 epochs.

LQ. For CIFAR10, we use learning rate (lr) as 0.1, momentum as 0.9, and weight decay as 1.0e-4. Learning rate scheduler (lrsch) is set to MultiStepLR of torch.optim.lr_scheduler with milestones of [82, 123]. Batch size is 128 and each model is trained for 200 epochs.

For ImageNet, we use learning rate (lr) as 0.01, momentum as 0.9, and weight decay as 1.0e-4. Learning rate scheduler (lrsch) is set to MultiStepLR of torch.optim.lr_scheduler with milestones of [10, 30, 60, 80,

95, 105]. Batch size is 256 and each model is trained for 120 epochs.

A.2.3. TTA

NORM [28, 31] For all experiments, we let each model see 64 samples for each batch at test-time.

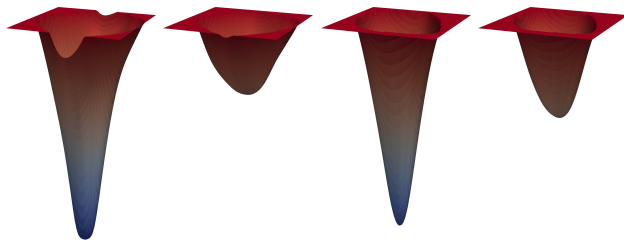
Tent [34] For CIFAR10 experiments, we utilize Adam optimizer with a learning rate of 0.001. For ImageNet experiments, we utilize an SGD optimizer with a learning rate of 0.00025. We follow the hyperparameter from the original paper [34]. We use 64 as the batch size for both datasets.

SAR [30] For both CIFAR10 and ImageNet experiments, we utilize SGD optimizer as the base optimizer of SAM [11] with a learning rate of 0.00025 and the threshold for filtering samples E_0 of $0.4 \times \ln 1000$ using batch size 64, following the original paper [30].

CoTTA [38] For both CIFAR-10 and ImageNet experiments, we utilize Adam optimizer with a learning rate of 0.001, 32 augmentations, and restoration probability p of 0.01, following the original paper [38].

B. Loss Landscape

We visualize the loss landscapes of the full precision (FP) models comparing them to those of QAT models shown in Figure 4 of Section 3.2.2. FP models show a smoother surface due to no quantization. The relative positions of the optima match the accuracy results from Tables 1 and 2. Unlike QAT models, full-precision models show no concave regions. For both cases tested on clean and corrupted images, the landscapes of the LFC-trained model (Figures 8a and 8b) tend to be sharper compared to those of the FFC-trained model (Figures 8c and 8d), which is the opposite for QAT models. This indicates that FP models may gain less benefits from LFC-training compared to QAT models.



(a) FFC Clean (b) FFC Corrupt. (c) LFC Clean (d) LFC Corrupt.
Figure 8. The loss landscapes of full precision ResNet26 on CIFAR10 (Clean) and CIFAR10-C (Corrupt.) trained on different frequency ranges. FFC refers to the full frequency of test data; LFC refers to lower frequency range in low pass filter of radius 8. We use visualization method following previous works [11, 26].

C. Choice of Frequency Filtering Radius for Low-frequency QAT

To determine the appropriate frequency range for the radius r in *LPF* (low-pass filtering), we conduct a frequency analysis on each dataset (i.e., CIFAR10 and ImageNet) in Sec 3.2.1. As radius r increases up to half of the input image size, the evaluation accuracy of the LFC-trained model on the uncorrupted test set converges to that of the FFC-trained model. The choices of radii r depend on the input size, which vary across datasets (i.e., 224 for ImageNet and 32 for CIFAR10). Therefore, we set the radius r to represent the same proportion of the input size for each dataset. The corresponding rows in the tables of Sec 3.2.1 indicate these proportional values across datasets. Finally, to ensure that *LPF* preserves a more robust and lower frequency range, we set $r=8$ for CIFAR10 and $r=56$ for ImageNet.

D. Evaluation Details

We provide per corruption results for Tables 4 and 5 of Sec 4. Results for default TTA baselines and *CoDA* are shown in Tables 11, 12 and 15. Results for *CoDA* enhanced methods are shown in Tables 13 and 14.

E. Model Size Calculation

We define model size as the number of bits that the model takes. As shown in Table 16, *CoDA* (Ours) on QAT models outperform the majority of TTA methods applied to the much larger FP models. For example, a ResNet18 model contains approximately 11 million parameters, meaning the 32-bit full-precision model size is about 374 million bits, while its 2-bit quantized counterpart is about 23 million bits, which is approximately 16 times smaller. Table 16 shows the total number of bits of our implemented models. The values in Fig 1 are from Table 16.

F. Inter-domain Distance Calculation

To compare how domain-invariant the LFC and HFC are, we calculate the inter-domain distances for each and constructed a matrix based on these values. From the CIFAR10-C dataset, we select one class and randomly choose a single uncorrupted original image from this class, along with its corresponding 15 corrupted versions. Each corrupted image is transformed into frequency domain features using FFT. We then apply LPF and HPF to these frequency domain features, extracting LFC and HFC in frequency domain, respectively. To quantify the variation of LFC and HFC features across different domains, we calculate the cosine distances separately between the LFC features and between the HFC features of images with different corruptions. This results in a 15×15 matrix for each feature type. We repeat this process for 10 randomly selected

Table 10. FABN improves TTA baselines and complements DeepAug under quantization on ImageNet-C. TTAs are conducted after DeepAug.

	ResNet18		ResNet50	
	FP	LSQ (2bit)	FP	LSQ (2bit)
<i>NoDeepAug</i>	22.36	16.25	27.74	19.76
<i>DeepAug</i>	41.29	27.74	51.91	32.97
NORM	49.82	36.72	58.59	42.53
+ <i>CoDA</i>	-	42.13	-	46.74
TENT	50.71	39.42	59.24	44.45
+ <i>CoDA</i>	-	42.44	-	46.97
SAR	54.24	42.27	57.14	46.70
+ <i>CoDA</i>	-	39.94	-	47.62

samples within the same class, averaging their resulting matrices. Finally, we perform this procedure for all classes, obtaining the overall inter-domain cosine distance matrix. A distance matrix with larger values indicates that the corresponding frequency component exhibits greater variability across domains. According to our resulting distance matrix presented in Figure 3, the values in the LFC distance matrix are relatively small, indicating that the LFC is more domain-invariant compared to the HFC.

G. Applicability to Domain Generalization methods

Table 10 show that *CoDA* remains orthogonal and complementary to not only widely-used TTA but also domain generalization (DG) methods. In all tested scenarios on ImageNet-C, *CoDA* consistently improves TTA baselines under low-bit quantization. Remarkably, in the ResNet-50 LSQ (2bit) setting, *CoDA* achieves 47.62%, outperforming full-precision models with TTA by up to 5.09%p. On ResNet-18, *CoDA* enhances methods like TENT and SAR, with improvements of +3.02%p and +5.35%p, respectively, compared to their quantized counterparts. These results highlight that *CoDA* further boosts accuracy when combined with a strong DG baseline, underscoring its distinct contribution.

H. License of Assets

Datasets CIFAR10 (MIT License), CIFAR10-C (Apache 2.0), ImageNet-C (Apache 2.0), ImageNet-R (MIT License), ImageNet-Sketch (MIT License)

Codes Code for Fourier transformation and low-/high-pass filtering of EfficientTrain (MIT License), torchvision for ResNet18 and ResNet50 (Apache 2.0), official repository of LQ (MIT License), official repository of TENT (MIT License), official repository of SAR (BSD 3-Clause License), and the official repository of CoTTA (MIT License).

Table 11. Average classification accuracy (%) and their standard deviations on ImageNet-C by ResNet18, shown per corruption, QAT, and TTA method. Averaged over three runs.

QAT	TTA	Gaussian	Shot	Impulse	Defocus	Glass	Motion	Zoom	Snow	Frost	Fog	Brightness	Contrast	Elastic	Pixelate	JPEG	Avg
FP	w/o TTA	10.59 ±0.00	10.58 ±0.00	10.08 ±0.00	16.18 ±0.00	10.26 ±0.01	18.35 ±0.00	20.29 ±0.00	17.01 ±0.00	14.46 ±0.00	25.94 ±0.00	47.60 ±0.00	21.89 ±0.00	37.48 ±0.00	36.37 ±0.00	38.25 ±0.00	22.36
	NORM	21.07 ±0.08	20.81 ±0.11	20.08 ±0.01	16.69 ±0.11	13.04 ±0.03	23.97 ±0.12	25.28 ±0.05	24.66 ±0.07	21.27 ±0.05	37.29 ±0.08	50.64 ±0.08	38.74 ±0.06	42.87 ±0.05	41.01 ±0.12	39.59 ±0.01	29.13
	Tent	22.92 ±0.18	22.40 ±0.12	20.61 ±0.05	18.44 ±0.15	15.28 ±0.14	29.05 ±0.06	28.73 ±0.05	24.86 ±0.05	21.18 ±0.14	39.50 ±0.20	50.37 ±0.10	40.49 ±0.07	44.83 ±0.11	42.12 ±0.02	38.51 ±0.16	30.62
	SAR	27.85 ±0.04	27.26 ±0.06	25.86 ±0.09	22.36 ±0.15	19.57 ±0.24	32.28 ±0.13	31.55 ±0.08	28.37 ±0.05	24.05 ±0.04	42.21 ±0.24	51.14 ±0.02	42.76 ±0.19	46.66 ±0.13	44.36 ±0.06	41.93 ±0.06	33.88
LSQ (2-bit)	w/o TTA	4.22 ±0.00	4.15 ±0.00	3.79 ±0.00	10.27 ±0.00	7.86 ±0.00	13.75 ±0.00	16.73 ±0.00	10.72 ±0.00	9.24 ±0.00	14.03 ±0.00	41.11 ±0.00	10.57 ±0.00	39.23 ±0.00	25.26 ±0.00	32.80 ±0.00	16.25
	NORM	16.27 ±0.01	15.92 ±0.08	15.44 ±0.14	9.44 ±0.10	11.89 ±0.05	18.26 ±0.02	21.90 ±0.12	19.04 ±0.05	18.40 ±0.10	27.15 ±0.08	45.82 ±0.09	27.04 ±0.11	44.09 ±0.07	38.49 ±0.10	37.44 ±0.15	24.44
	Tent	23.34 ±0.07	20.96 ±0.02	20.40 ±0.11	15.35 ±0.06	16.36 ±0.16	23.39 ±0.09	27.01 ±0.03	19.44 ±0.16	18.73 ±0.03	30.73 ±0.16	46.07 ±0.05	30.37 ±0.00	45.17 ±0.18	40.29 ±0.28	38.51 ±0.05	27.74
	SAR	25.52 ±0.07	23.49 ±0.13	22.76 ±0.18	17.56 ±0.19	18.73 ±0.27	25.79 ±0.16	28.65 ±0.15	21.00 ±0.08	19.87 ±0.04	33.12 ±0.16	46.22 ±0.03	32.96 ±0.10	45.52 ±0.12	41.32 ±0.11	39.58 ±0.14	29.47
	CoDA (Ours)	27.68 ±0.04	24.62 ±0.08	25.05 ±0.03	20.87 ±0.05	21.30 ±0.06	27.60 ±0.02	29.63 ±0.09	20.30 ±0.13	21.10 ±0.03	33.51 ±0.06	47.33 ±0.11	34.94 ±0.09	47.29 ±0.08	47.51 ±0.02	42.77 ±0.05	31.43
LQ (2-bit)	w/o TTA	7.67 ±0.00	7.75 ±0.00	6.67 ±0.00	12.26 ±0.00	10.80 ±0.00	16.53 ±0.00	17.86 ±0.00	13.33 ±0.00	10.80 ±0.00	13.96 ±0.00	43.70 ±0.00	9.45 ±0.00	41.69 ±0.00	29.29 ±0.00	38.20 ±0.00	18.66
	NORM	19.45 ±0.06	18.86 ±0.04	18.02 ±0.03	14.55 ±0.16	15.15 ±0.12	23.46 ±0.12	25.65 ±0.03	22.87 ±0.10	21.11 ±0.03	33.92 ±0.11	48.63 ±0.18	35.67 ±0.07	45.85 ±0.08	39.79 ±0.07	42.28 ±0.09	28.35
	Tent	23.73 ±0.17	21.76 ±0.12	21.33 ±0.10	17.68 ±0.13	18.30 ±0.11	27.56 ±0.03	29.00 ±0.08	23.56 ±0.10	21.65 ±0.08	36.57 ±0.17	48.38 ±0.05	36.93 ±0.04	46.44 ±0.09	41.44 ±0.02	42.01 ±0.11	30.42
	SAR	23.67 ±0.15	21.75 ±0.04	21.30 ±0.15	17.67 ±0.11	18.18 ±0.09	27.49 ±0.14	28.93 ±0.08	23.61 ±0.09	21.64 ±0.12	36.62 ±0.16	48.32 ±0.10	37.00 ±0.17	46.52 ±0.13	41.51 ±0.16	42.02 ±0.10	30.42
	CoDA (Ours)	30.58 ±0.11	29.15 ±0.14	28.43 ±0.03	22.11 ±0.11	22.52 ±0.07	31.64 ±0.16	31.93 ±0.04	25.82 ±0.10	24.98 ±0.10	37.92 ±0.04	49.03 ±0.02	38.95 ±0.03	47.75 ±0.03	47.80 ±0.16	45.48 ±0.09	34.27
LSQ (4-bit)	w/o TTA	6.76 ±0.01	6.97 ±0.00	5.96 ±0.01	12.06 ±0.00	9.53 ±0.00	16.05 ±0.02	19.21 ±0.00	14.76 ±0.02	13.07 ±0.01	19.53 ±0.01	45.94 ±0.01	15.46 ±0.01	39.99 ±0.00	35.75 ±0.02	37.54 ±0.02	19.91
	NORM	19.74 ±0.57	19.28 ±0.74	18.93 ±0.77	13.21 ±1.40	14.19 ±1.44	22.80 ±1.79	25.55 ±0.87	23.63 ±0.62	21.69 ±0.14	33.40 ±0.85	49.38 ±0.15	37.00 ±0.56	45.94 ±0.81	42.06 ±0.06	40.65 ±0.75	28.50
	Tent	24.65 ±0.05	22.31 ±0.09	21.50 ±0.06	18.09 ±0.02	16.98 ±0.04	27.94 ±0.10	29.55 ±0.12	23.63 ±0.03	21.54 ±0.02	35.47 ±0.07	49.73 ±0.21	37.82 ±0.22	46.85 ±0.11	43.75 ±0.12	41.10 ±0.01	30.73
	SAR	26.06 ±0.03	24.23 ±0.13	23.21 ±0.07	19.52 ±0.07	18.43 ±0.04	29.31 ±0.04	30.53 ±0.12	24.91 ±0.11	22.36 ±0.07	36.97 ±0.05	49.99 ±0.12	38.97 ±0.13	47.14 ±0.16	44.42 ±0.13	41.94 ±0.11	31.87
	CoDA (Ours)	28.18 ±0.04	26.41 ±0.01	25.19 ±0.05	22.11 ±0.04	21.12 ±0.05	30.69 ±0.05	31.48 ±0.06	23.67 ±0.03	23.27 ±0.10	36.70 ±0.04	50.26 ±0.05	40.09 ±0.10	48.89 ±0.13	49.87 ±0.07	44.55 ±0.01	33.50
LQ (4-bit)	w/o TTA	6.96 ±0.00	6.81 ±0.00	6.23 ±0.00	15.48 ±0.03	10.99 ±0.02	19.37 ±0.01	20.91 ±0.00	15.71 ±0.01	12.70 ±0.00	20.65 ±0.01	45.28 ±0.01	16.12 ±0.02	42.19 ±0.00	37.44 ±0.03	36.56 ±0.01	20.89
	NORM	19.33 ±0.70	18.94 ±0.71	18.47 ±0.74	14.09 ±1.49	14.91 ±1.40	23.76 ±1.72	26.10 ±1.02	24.07 ±0.74	21.56 ±0.07	33.92 ±0.93	49.28 ±0.06	37.30 ±0.57	46.22 ±0.79	42.12 ±0.07	40.11 ±0.73	28.68
	Tent	21.55 ±0.17	20.21 ±0.10	18.52 ±0.09	17.65 ±0.04	17.80 ±0.02	29.01 ±0.08	29.49 ±0.07	24.17 ±0.09	20.69 ±0.10	36.47 ±0.05	48.93 ±0.10	37.78 ±0.21	47.12 ±0.12	42.58 ±0.05	39.03 ±0.16	30.07
	SAR	21.53 ±0.16	20.20 ±0.11	18.55 ±0.06	17.67 ±0.06	17.79 ±0.06	29.02 ±0.10	29.50 ±0.05	24.14 ±0.11	20.70 ±0.03	36.40 ±0.02	48.93 ±0.04	37.80 ±0.21	47.15 ±0.12	42.55 ±0.13	39.06 ±0.07	30.07
	CoDA (Ours)	29.02 ±0.05	27.89 ±0.06	25.92 ±0.05	24.77 ±0.07	23.50 ±0.05	32.86 ±0.10	32.54 ±0.07	25.72 ±0.04	24.52 ±0.08	38.28 ±0.09	49.89 ±0.06	40.92 ±0.03	48.66 ±0.12	48.60 ±0.05	43.85 ±0.03	34.46
LSQ (8-bit)	w/o TTA	5.77 ±0.00	6.06 ±0.01	4.95 ±0.01	12.26 ±0.01	10.14 ±0.01	16.67 ±0.01	20.05 ±0.01	15.66 ±0.01	13.44 ±0.00	20.07 ±0.00	45.94 ±0.01	15.47 ±0.01	39.12 ±0.02	38.64 ±0.02	37.93 ±0.00	20.14
	NORM	20.66 ±0.06	20.20 ±0.03	20.28 ±0.02	14.53 ±0.06	14.60 ±0.10	23.77 ±0.10	26.15 ±0.12	24.14 ±0.11	22.26 ±0.07	35.12 ±0.11	49.67 ±0.07	37.42 ±0.13	45.25 ±0.09	43.11 ±0.15	41.35 ±0.17	29.23
	Tent	24.76 ±0.02	22.45 ±0.06	21.89 ±0.07	17.55 ±0.14	17.93 ±0.05	28.98 ±0.10	29.94 ±0.05	24.41 ±0.16	22.37 ±0.03	36.75 ±0.08	50.09 ±0.07	38.38 ±0.08	46.75 ±0.12	44.45 ±0.11	42.00 ±0.05	31.25
	SAR	26.24 ±0.02	23.94 ±0.06	23.38 ±0.05	18.77 ±0.09	19.01 ±0.06	29.96 ±0.05	30.62 ±0.09	25.32 ±0.19	23.06 ±0.02	37.87 ±0.10	50.24 ±0.06	39.03 ±0.06	47.03 ±0.08	44.91 ±0.15	42.62 ±0.06	32.13
	CoDA (Ours)	29.03 ±0.07	27.36 ±0.09	26.59 ±0.11	21.38 ±0.06	22.19 ±0.03	32.09 ±0.06	32.19 ±0.04	24.71 ±0.10	24.17 ±0.07	37.88 ±0.03	50.61 ±0.09	40.70 ±0.04	48.33 ±0.08	50.01 ±0.05	45.30 ±0.05	34.17
LQ (8-bit)	w/o TTA	6.09 ±0.01	6.57 ±0.00	5.85 ±0.01	15.56 ±0.00	10.70 ±0.00	19.41 ±0.00	21.17 ±0.01	16.58 ±0.00	12.99 ±0.01	22.22 ±0.02	46.81 ±0.01	17.29 ±0.01	42.13 ±0.01	36.61 ±0.00	36.62 ±0.00	21.11
	NORM	20.44 ±0.05	20.17 ±0.02	19.85 ±0.07	16.26 ±0.03	15.71 ±0.08	24.97 ±0.10	27.66 ±0.04	26.77 ±0.11	23.52 ±0.02	38.29 ±0.02	51.45 ±0.06	39.86 ±0.05	47.65 ±0.02	42.69 ±0.03	40.94 ±0.03	30.42
	Tent	22.70 ±0.06	21.10 ±0.05	19.77 ±0.05	18.41 ±0.07	17.19 ±0.11	29.97 ±0.15	30.66 ±0.09	27.02 ±0.06	22.92 ±0.06	40.11 ±0.18	51.65 ±0.03	40.34 ±0.11	49.16 ±0.12	43.97 ±0.11	40.68 ±0.08	31.71
	SAR	22.71 ±0.07	21.12 ±0.06	19.77 ±0.07	18.36 ±0.11	17.16 ±0.10	29.91 ±0.11	30.62 ±0.00	27.04 ±0.06	22.92 ±0.06	40.11 ±0.16	51.66 ±0.04	40.35 ±0.10	49.15 ±0.11	43.97 ±0.11	40.67 ±0.09	31.70
	CoDA (Ours)	28.82 ±0.16	27.93 ±0.06	26.05 ±0.15	25.05 ±0.32	23.69 ±0.13	32.84 ±0.03	32.56 ±0.06	25.77 ±0.04	24.67 ±0.20	38.50 ±0.12	49.69 ±0.23	40.95 ±0.01	48.50 ±0.24	49.12 ±0.06	42.99 ±0.05	34.48

Table 12. Average classification accuracy (%) and their standard deviations on ImageNet-C by ResNet50, shown per corruption, QAT, and TTA method. Averaged over three runs.

QAT	TTA	Gaussian	Shot	Impulse	Defocus	Glass	Motion	Zoom	Snow	Frost	Fog	Brightness	Contrast	Elastic	Pixelate	JPEG	Avg
FP	w/o TTA	15.45 ±0.00	14.99 ±0.00	14.50 ±0.00	21.22 ±0.00	12.66 ±0.00	23.18 ±0.00	24.82 ±0.00	22.47 ±0.00	20.50 ±0.00	32.61 ±0.00	55.83 ±0.00	28.78 ±0.00	42.44 ±0.00	40.03 ±0.00	46.62 ±0.00	27.74
	NORM	29.10 ±0.08	27.62 ±0.08	27.77 ±0.08	23.05 ±0.11	18.37 ±0.05	30.56 ±0.09	31.97 ±0.02	31.51 ±0.05	27.80 ±0.03	45.39 ±0.10	58.67 ±0.06	46.66 ±0.06	49.78 ±0.10	48.17 ±0.10	46.53 ±0.11	36.20
	Tent	31.57 ±0.19	31.30 ±0.19	29.71 ±0.03	25.52 ±0.06	21.16 ±0.07	36.49 ±0.07	36.73 ±0.02	33.02 ±0.13	28.02 ±0.16	48.36 ±0.03	58.47 ±0.06	49.07 ±0.11	53.02 ±0.07	49.55 ±0.06	46.24 ±0.09	38.55
	SAR	35.76 ±0.11	35.82 ±0.15	34.79 ±0.25	29.21 ±0.10	25.87 ±0.10	39.85 ±0.10	39.08 ±0.19	36.52 ±0.08	30.56 ±0.12	50.19 ±0.06	58.84 ±0.03	50.55 ±0.07	54.38 ±0.04	51.91 ±0.09	48.92 ±0.12	41.48
LSQ (2-bit)	w/o TTA	5.22 ±0.00	5.21 ±0.00	4.54 ±0.00	13.74 ±0.00	10.31 ±0.00	17.77 ±0.00	20.79 ±0.00	13.83 ±0.00	12.05 ±0.00	16.79 ±0.00	46.77 ±0.00	13.09 ±0.00	44.00 ±0.01	33.59 ±0.01	38.69 ±0.00	19.76
	NORM	21.69 ±0.16	21.06 ±0.02	20.55 ±0.07	14.58 ±0.11	16.98 ±0.07	24.17 ±0.05	28.22 ±0.02	24.66 ±0.02	23.53 ±0.04	34.13 ±0.24	51.83 ±0.06	35.37 ±0.13	50.30 ±0.04	46.10 ±0.09	43.48 ±0.11	30.44
	Tent	23.16 ±0.13	22.79 ±0.10	21.13 ±0.03	21.81 ±0.06	21.84 ±0.12	30.37 ±0.12	33.47 ±0.05	25.10 ±0.10	24.07 ±0.03	37.65 ±0.05	52.28 ±0.11	39.13 ±0.12	51.12 ±0.03	47.13 ±0.14	44.33 ±0.11	33.03
	SAR	25.03 ±0.14	24.62 ±0.04	22.95 ±0.12	23.08 ±0.22	22.91 ±0.10	31.39 ±0.15	34.07 ±0.11	26.26 ±0.17	24.60 ±0.16	38.66 ±0.04	52.45 ±0.05	40.04 ±0.12	51.36 ±0.04	47.69 ±0.14	45.12 ±0.11	34.02
	CoDA (Ours)	23.84 ±0.08	24.04 ±0.08	22.45 ±0.11	26.97 ±0.09	25.46 ±0.02	33.59 ±0.03	35.33 ±0.15	25.07 ±0.11	25.07 ±0.09	38.52 ±0.07	52.77 ±0.09	41.59 ±0.06	52.56 ±0.02	53.04 ±0.08	48.05 ±0.08	35.22
LQ (2-bit)	w/o TTA	8.89 ±0.01	8.95 ±0.01	8.19 ±0.00	17.25 ±0.00	11.49 ±0.00	21.72 ±0.00	25.12 ±0.01	17.67 ±0.00	13.33 ±0.01	21.14 ±0.01	49.39 ±0.00	15.66 ±0.00	43.98 ±0.00	30.58 ±0.00	40.11 ±0.00	22.23
	NORM	22.57 ±0.08	22.06 ±0.04	21.72 ±0.06	18.28 ±0.13	18.21 ±0.11	27.56 ±0.08	30.87 ±0.14	28.76 ±0.08	25.36 ±0.11	38.23 ±0.12	54.74 ±0.19	40.91 ±0.08	50.61 ±0.17	46.47 ±0.15	43.39 ±0.07	32.65
	Tent	25.09 ±0.13	24.95 ±0.22	23.25 ±0.15	23.35 ±0.02	21.45 ±0.07	32.95 ±0.07	35.15 ±0.17	29.32 ±0.02	26.15 ±0.08	41.38 ±0.17	54.74 ±0.05	43.22 ±0.10	52.02 ±0.01	47.99 ±0.04	44.41 ±0.15	35.03
	SAR	25.10 ±0.14	24.93 ±0.16	23.13 ±0.05	23.37 ±0.08	21.49 ±0.01	32.96 ±0.11	35.16 ±0.10	29.31 ±0.05	26.14 ±0.08	41.39 ±0.15	54.79 ±0.10	43.25 ±0.14	52.07 ±0.03	48.04 ±0.03	44.44 ±0.03	35.04
	CoDA (Ours)	27.84 ±0.12	28.44 ±0.14	26.56 ±0.04	28.97 ±0.02	25.80 ±0.18	36.21 ±0.07	37.57 ±0.04	28.71 ±0.02	27.63 ±0.07	42.81 ±0.18	55.25 ±0.13	47.05 ±0.11	53.87 ±0.09	54.47 ±0.09	48.97 ±0.05	38.01
LSQ (4-bit)	w/o TTA	5.88 ±0.01	6.08 ±0.01	4.92 ±0.02	14.97 ±0.01	10.95 ±0.01	19.02 ±0.00	22.21 ±0.01	16.03 ±0.03	14.49 ±0.01	21.62 ±0.01	49.34 ±0.01	17.09 ±0.01	43.32 ±0.02	36.62 ±0.01	40.99 ±0.04	21.57
	NORM	22.83 ±0.07	21.91 ±0.08	22.02 ±0.06	16.30 ±0.06	16.24 ±0.06	25.44 ±0.05	28.35 ±0.07	25.81 ±0.04	23.83 ±0.09	35.26 ±0.17	53.10 ±0.03	39.36 ±0.03	49.28 ±0.09	45.41 ±0.13	44.41 ±0.01	31.30
	Tent	26.47 ±0.06	25.48 ±0.11	23.83 ±0.08	21.06 ±0.07	19.79 ±0.04	30.67 ±0.11	32.23 ±0.03	26.25 ±0.06	23.92 ±0.08	38.77 ±0.09	53.53 ±0.20	41.34 ±0.04	50.33 ±0.05	47.00 ±0.09	44.78 ±0.08	33.70
	SAR	27.62 ±0.16	26.70 ±0.07	25.11 ±0.11	21.69 ±0.09	20.63 ±0.08	31.44 ±0.12	32.86 ±0.03	27.07 ±0.03	24.42 ±0.08	39.56 ±0.07	53.59 ±0.12	41.86 ±0.07	50.63 ±0.06	47.49 ±0.21	45.37 ±0.05	34.40
	CoDA (Ours)	29.96 ±0.05	29.41 ±0.19	27.61 ±0.06	25.11 ±0.01	23.03 ±0.02	33.81 ±0.08	33.99 ±0.12	25.59 ±0.06	25.56 ±0.06	39.01 ±0.13	53.91 ±0.08	43.28 ±0.14	51.82 ±0.02	53.33 ±0.04	48.29 ±0.10	36.25
LQ (4-bit)	w/o TTA	10.33 ±0.01	10.02 ±0.01	9.85 ±0.01	16.63 ±0.02	12.10 ±0.03	19.98 ±0.03	24.01 ±0.00	17.56 ±0.06	14.04 ±0.03	23.34 ±0.01	49.37 ±0.01	18.56 ±0.01	43.47 ±0.05	34.93 ±0.02	40.23 ±0.01	22.96
	NORM	22.35 ±0.08	21.82 ±0.09	21.40 ±0.08	18.09 ±0.11	16.76 ±0.13	26.32 ±0.07	29.91 ±0.07	27.24 ±0.08	24.47 ±0.18	36.92 ±0.13	54.01 ±0.11	41.60 ±0.07	49.59 ±0.14	45.11 ±0.08	43.36 ±0.06	31.93
	Tent	25.34 ±0.18	25.31 ±0.08	23.27 ±0.13	21.33 ±0.06	19.10 ±0.05	31.60 ±0.17	33.19 ±0.10	27.69 ±0.06	24.81 ±0.12	40.11 ±0.09	53.84 ±0.10	42.94 ±0.04	50.44 ±0.06	47.05 ±0.06	43.36 ±0.07	33.96
	SAR	25.29 ±0.06	25.27 ±0.05	23.17 ±0.17	21.36 ±0.09	19.16 ±0.08	31.63 ±0.06	33.13 ±0.12	27.61 ±0.04	24.80 ±0.12	40.09 ±0.07	53.81 ±0.09	42.94 ±0.06	50.47 ±0.07	47.07 ±0.05	43.39 ±0.02	33.95
	CoDA (Ours)	28.82 ±0.11	28.99 ±0.08	26.30 ±0.24	26.19 ±0.08	22.97 ±0.15	34.54 ±0.14	35.00 ±0.08	26.69 ±0.18	25.83 ±0.12	40.57 ±0.15	54.01 ±0.06	45.24 ±0.17	51.47 ±0.24	53.23 ±0.17	47.53 ±0.14	36.49
LSQ (8-bit)	w/o TTA	7.03 ±0.01	6.79 ±0.03	6.20 ±0.00	15.63 ±0.01	11.69 ±0.01	19.68 ±0.00	22.38 ±0.01	17.40 ±0.01	15.50 ±0.01	22.26 ±0.01	49.14 ±0.01	18.45 ±0.02	44.20 ±0.01	40.63 ±0.00	41.77 ±0.01	22.58
	NORM	23.72 ±0.04	23.31 ±0.05	22.40 ±0.07	16.92 ±0.01	16.66 ±0.12	26.24 ±0.06	28.47 ±0.04	26.41 ±0.11	24.18 ±0.06	36.36 ±0.09	52.86 ±0.12	39.79 ±0.08	49.16 ±0.12	46.96 ±0.06	44.62 ±0.03	31.87
	Tent	28.32 ±0.06	27.43 ±0.08	25.94 ±0.05	20.27 ±0.16	19.86 ±0.12	30.76 ±0.14	31.87 ±0.06	26.90 ±0.07	24.39 ±0.04	39.11 ±0.09	53.34 ±0.06	40.18 ±0.07	50.28 ±0.05	47.88 ±0.15	45.18 ±0.09	34.11
	SAR	29.28 ±0.14	28.43 ±0.09	27.07 ±0.08	21.26 ±0.11	20.88 ±0.04	31.59 ±0.13	32.66 ±0.14	27.76 ±0.05	25.06 ±0.05	40.12 ±0.03	53.48 ±0.11	40.86 ±0.05	50.59 ±0.04	48.25 ±0.10	45.71 ±0.12	34.87
	CoDA (Ours)	32.11 ±0.05	31.25 ±0.08	30.07 ±0.03	23.54 ±0.07	23.45 ±0.03	33.78 ±0.19	34.17 ±0.02	26.09 ±0.09	25.67 ±0.08	39.03 ±0.04	53.89 ±0.09	42.80 ±0.09	52.06 ±0.06	53.81 ±0.03	48.43 ±0.09	36.68
LQ (8-bit)	w/o TTA	2.81 ±0.01	3.31 ±0.00	2.86 ±0.00	6.46 ±0.02	7.48 ±0.01	10.34 ±0.00	10.55 ±0.02	9.94 ±0.01	5.52 ±0.01	15.24 ±0.01	34.63 ±0.01	11.91 ±0.00	27.05 ±0.01	25.73 ±0.01	27.86 ±0.01	13.45
	NORM	17.15 ±0.06	17.11 ±0.03	16.70 ±0.04	12.85 ±0.09	13.87 ±0.05	18.56 ±0.05	19.20 ±0.03	23.38 ±0.06	21.09 ±0.05	29.85 ±0.07	43.86 ±0.06	27.56 ±0.04	35.68 ±0.04	32.42 ±0.07	31.93 ±0.12	24.08
	Tent	24.80 ±0.00	24.58 ±0.05	22.17 ±0.06	17.26 ±0.09	16.68 ±0.12	25.15 ±0.08	25.12 ±0.05	27.65 ±0.08	23.48 ±0.07	37.05 ±0.07	47.30 ±0.07	33.35 ±0.05	43.00 ±0.10	39.25 ±0.03	37.68 ±0.05	29.63
	SAR	24.75 ±0.06	24.59 ±0.03	22.16 ±0.06	17.25 ±0.11	16.67 ±0.11	25.13 ±0.06	25.13 ±0.04	27.65 ±0.08	23.48 ±0.07	37.04 ±0.06	47.28 ±0.07	33.33 ±0.05	43.00 ±0.11	39.26 ±0.01	37.68 ±0.05	29.63
	CoDA (Ours)	31.78 ±0.06	31.97 ±0.06	29.79 ±0.11	26.51 ±0.01	25.25 ±0.07	33.70 ±0.07	32.31 ±0.03	27.41 ±0.05	25.70 ±0.14	39.01 ±0.05	47.88 ±0.13	37.41 ±0.14	46.46 ±0.06	46.83 ±0.08	43.27 ±0.01	35.02

Table 13. Average classification accuracy (%) on ImageNet-C by ResNet18, shown per corruption, QAT, and TTA method.

QAT	TTA	gaus	shot	impul	defcs	gls	mtn	zm	snow	frost	fog	brt	cnt	els	px	jpg	AVG
FP	w/o TTA	10.59	10.58	10.08	18.26	10.26	18.35	20.29	17.01	14.46	25.94	21.89	37.26	47.60	36.37	38.25	22.36
	NORM	20.98	20.97	20.07	16.72	13.02	23.84	25.24	19.73	24.58	21.23	37.26	50.63	48.00	42.83	40.87	29.09
	TENT	22.72	22.53	20.58	18.26	15.13	29.06	31.54	28.48	21.21	21.59	44.43	49.11	44.82	42.13	38.61	30.61
	SAR	27.82	27.19	25.76	22.21	19.83	31.51	35.33	20.38	25.49	28.50	41.66	51.16	46.67	44.24	41.15	33.91
LSQ (2-bit)	w/o TTA	4.22	4.15	3.79	10.57	7.86	13.75	15.73	10.72	9.24	14.03	19.43	39.23	39.28	25.26	32.80	16.25
	CODA	27.69	24.57	25.06	20.88	21.28	27.62	29.73	20.38	21.13	33.45	47.37	47.53	46.77	46.95	42.71	31.45
	SAR + CODA	27.79	24.85	25.23	21.19	21.62	28.16	29.89	20.63	21.42	34.10	47.42	47.59	42.89	47.77	42.82	31.73
	TENT + CODA	25.63	23.34	25.07	21.44	21.01	29.02	29.99	19.97	20.38	21.13	34.14	46.79	46.77	46.95	42.66	31.22
LQ (2-bit)	w/o TTA	7.67	7.75	6.67	12.26	10.80	16.53	17.86	13.33	10.80	13.96	43.70	9.45	41.69	29.29	38.20	18.66
	CODA	30.45	28.99	28.46	22.23	22.58	31.83	31.98	25.88	25.09	37.90	48.99	38.98	47.77	47.63	45.47	34.28
	SAR + CODA	30.45	28.97	28.49	22.23	22.59	31.81	32.04	25.91	25.09	37.93	48.99	38.93	47.79	47.69	45.48	34.29
	TENT + CODA	30.46	29.05	28.39	22.23	22.37	31.73	31.91	25.85	24.91	37.70	48.80	38.52	47.76	47.53	45.36	34.17
LSQ (4-bit)	w/o TTA	6.75	6.97	5.98	12.06	9.53	16.03	19.21	14.78	13.06	19.52	45.93	15.47	39.98	35.77	37.56	19.91
	CODA	28.15	26.40	25.14	22.14	21.16	30.66	31.41	23.69	23.24	36.75	50.32	40.08	48.79	49.90	44.56	33.49
	SAR + CODA	28.35	26.63	25.42	22.40	21.26	30.98	31.74	23.98	23.35	37.17	50.30	40.50	48.95	49.80	44.72	33.70
	TENT + CODA	28.10	26.49	25.23	23.00	21.14	31.21	31.50	23.42	22.65	37.14	49.93	41.02	48.54	49.47	44.63	33.56
LQ (4-bit)	w/o TTA	6.96	6.81	6.23	15.45	10.97	19.39	20.91	15.70	12.70	20.66	45.29	16.09	42.18	37.47	36.55	20.89
	CODA	29.00	27.96	25.97	24.79	23.52	32.76	32.48	25.76	24.53	38.27	49.92	40.93	48.67	48.55	43.89	34.47
	SAR + CODA	28.39	27.01	25.44	24.67	22.65	32.24	31.79	24.74	23.63	37.74	48.94	40.74	48.37	48.09	43.04	33.83
	TENT + CODA	28.39	26.70	25.30	24.69	22.47	32.38	31.77	24.69	23.40	37.68	48.89	40.34	48.17	47.84	42.97	33.71
LSQ (8-bit)	w/o TTA	5.77	6.07	4.94	12.25	10.15	16.66	20.06	15.65	13.44	20.07	45.95	15.46	39.15	38.62	37.94	20.15
	CODA	29.11	27.31	26.56	21.45	22.16	32.15	32.23	24.73	24.11	37.85	50.67	40.69	48.41	50.07	45.34	34.19
	SAR + CODA	29.26	27.77	26.88	21.76	22.38	32.25	32.42	25.01	24.48	38.27	50.76	40.85	48.51	50.08	45.39	34.40
	TENT + CODA	29.55	27.93	27.05	22.39	22.28	32.64	32.22	24.69	24.27	38.25	50.40	41.45	48.06	49.76	45.23	34.41
LQ (8-bit)	w/o TTA	6.10	6.57	5.86	15.56	10.70	19.41	21.16	16.58	13.00	22.20	46.82	17.28	42.12	36.61	36.62	21.11
	CODA	28.66	27.94	26.18	25.27	23.80	32.86	32.56	25.81	24.81	38.56	49.63	40.96	48.32	49.08	43.04	34.50
	SAR + CODA	28.70	27.93	26.20	25.18	23.76	32.85	32.58	25.68	24.77	38.66	49.46	40.90	48.41	48.98	42.97	34.47
	TENT + CODA	28.67	27.96	26.14	25.12	23.72	32.62	32.47	25.57	24.69	38.51	49.26	40.69	48.26	48.86	42.77	34.35

Table 14. Average classification accuracy (%) on ImageNet-C by ResNet50, shown per corruption, QAT, and TTA method.

QAT	TTA	gaus	shot	impul	defcs	gls	mtn	zm	snow	frost	fog	brt	cnt	els	px	jpg	AVG
FP	w/o TTA	15.45	14.99	14.5	21.22	12.66	23.18	24.82	22.47	20.50	32.61	55.83	28.78	42.44	40.03	46.62	27.74
	NORM	29.18	27.57	27.85	23.13	18.32	30.61	31.96	31.55	27.83	45.39	58.69	46.63	49.76	48.21	46.60	36.22
	TENT	31.69	31.10	29.68	25.57	21.10	36.41	36.71	32.98	28.2	48.39	58.48	48.99	52.94	49.56	46.22	38.53
	SAR	35.81	35.66	34.56	29.32	25.78	39.79	39.25	36.43	30.70	50.17	58.84	50.62	54.40	52.00	48.96	41.49
LSQ (2-bit)	w/o TTA	5.22	5.21	4.54	13.74	10.31	17.77	20.79	13.83	12.05	16.79	46.77	13.09	44.00	33.59	38.69	19.76
	CODA	23.77	24.13	22.55	27.07	25.44	33.57	35.45	25.13	24.98	38.57	52.84	41.54	52.55	52.99	48.13	35.25
	TENT + CODA	24.09	24.29	22.84	27.18	25.46	33.61	35.31	25.15	25.07	38.71	52.83	41.57	52.51	52.97	48.33	35.33
	SAR + CODA	24.92	25.19	23.07	27.88	25.88	34.32	35.54	25.48	25.16	39.68	52.80	42.53	52.68	52.98	48.52	35.78
LQ (2-bit)	w/o TTA	8.89	8.96	8.19	17.25	11.49	21.72	25.12	17.67	13.33	21.14	49.39	15.66	43.98	30.58	40.11	22.23
	CODA	27.87	28.51	26.53	28.96	25.88	36.14	37.57	28.70	27.71	42.77	55.40	47.01	53.79	54.57	49.02	38.03
	TENT + CODA	27.90	28.40	26.52	29.13	25.56	36.28	37.40	28.65	27.51	42.76	55.15	46.96	54.13	54.26	49.17	37.99
	SAR + CODA	27.97	28.47	26.46	28.98	25.76	35.95	37.34	28.50	27.50	42.60	54.97	46.61	53.99	54.37	49.04	37.90
LSQ (4-bit)	w/o TTA	5.89	6.09	4.89	14.98	10.96	19.02	22.22	16.07	14.48	21.61	49.35	17.10	43.34	36.63	40.95	21.57
	CODA	30.00	29.29	27.65	25.12	23.03	33.88	33.93	25.53	25.54	38.96	53.90	43.18	51.82	53.30	48.30	36.23
	TENT + CODA	30.12	29.60	27.96	25.10	23.11	34.08	34.09	25.84	25.70	39.13	53.96	43.37	51.94	53.36	48.45	36.39
	SAR + CODA	30.33	29.77	27.94	25.69	23.39	34.14	34.37	25.63	25.35	39.72	53.69	43.67	51.82	53.43	48.39	36.49
LQ (4-bit)	w/o TTA	10.34	10.02	9.84	16.65	12.13	19.95	24.01	17.62	14.01	23.33	49.38	18.57	43.41	34.95	40.24	22.96
	CODA	28.73	28.93	26.10	26.12	23.13	34.50	35.08	26.55	25.75	40.58	54.06	45.14	51.32	53.42	47.60	36.47
	TENT + CODA	28.39	27.01	25.44	24.67	22.65	32.24	31.79	24.74	23.63	37.74	48.94	40.74	48.37	48.09	43.04	33.83
	SAR + CODA	28.67	28.80	26.08	26.05	23.19	34.54	34.81	26.57	25.90	40.61	53.96	44.94	51.44	53.04	47.37	36.40
LSQ (8-bit)	w/o TTA	7.02	6.82	6.20	15.62	11.70	19.68	22.37	17.39	15.51	22.27	49.15	18.48	44.21	40.63	41.78	22.59
	CODA	32.06	31.28	30.04	23.47	23.44	33.72	34.19	26.04	25.63	39.02	53.86	42.74	52.12	53.79	48.36	36.65
	TENT + CODA	32.17	31.35	30.30	23.69	23.50	33.79	34.19	26.19	25.73	39.19	54.05	42.89	52.14	53.78	48.47	36.76
	SAR + CODA	32.16	31.45	30.26	24.09	23.60	33.80	34.13	26.16	25.39	39.20	53.76	43.05	51.99	53.53	48.34	36.73
LQ (8-bit)	w/o TTA	3.35	4.00	3.26	9.48	9.87	13.59	14.13	11.54	9.57	18.96	37.39	12.65	31.59	25.64	30.51	15.70
	CODA	33.36	33.18	31.55	25.58	25.51	32.70	33.38	26.71	25.80	38.85	47.63	37.19	46.77	46.81	43.08	35.21
	TENT + CODA	33.48	33.41	31.83	25.57	25.44	32.66	33.36	26.64	25.65	38.79	47.58	37.08	46.69	46.75	43.27	35.21
	SAR + CODA	33.45	33.30	31.77	25.59	25.34	32.55	33.20	26.46	25.49	38.63	47.35	36.88	46.50	46.62	43.16	35.09

Table 15. Average classification accuracy (%) and their standard deviations on CIFAR10-C by ResNet26, shown per corruption, QAT, and TTA method. Averaged over three runs.

QAT	TTA	<i>Gaussian</i>	<i>Shot</i>	<i>Impulse</i>	<i>Defocus</i>	<i>Glass</i>	<i>Motion</i>	<i>Zoom</i>	<i>Snow</i>	<i>Frost</i>	<i>Fog</i>	<i>Brightness</i>	<i>Contrast</i>	<i>Elastic</i>	<i>Pixelate</i>	<i>JPEG</i>	Avg
FP	w/o TTA	31.80 ±0.01	37.39 ±0.01	29.29 ±0.01	57.88 ±0.01	45.04 ±0.01	63.94 ±0.02	55.67 ±0.01	68.09 ±0.01	55.59 ±0.02	65.06 ±0.02	85.69 ±0.01	33.26 ±0.00	67.94 ±0.01	42.12 ±0.01	69.21 ±0.00	53.86
	NORM	58.59 ±0.14	60.87 ±0.12	51.62 ±0.07	73.24 ±0.16	55.21 ±0.21	75.02 ±0.02	71.96 ±0.10	72.19 ±0.02	68.49 ±0.18	76.85 ±0.15	86.12 ±0.09	60.38 ±0.22	71.75 ±0.18	66.17 ±0.06	70.73 ±0.19	67.95
	Tent	67.08 ±0.26	69.46 ±0.15	59.09 ±0.22	81.85 ±0.05	59.22 ±0.27	80.21 ±0.13	79.90 ±0.10	76.91 ±0.01	74.86 ±0.18	78.53 ±0.15	86.72 ±0.16	82.47 ±0.28	71.45 ±0.08	74.56 ±0.08	71.18 ±0.28	74.23
	SAR	65.67 ±0.15	68.19 ±0.17	57.81 ±0.28	81.02 ±0.12	58.08 ±0.07	79.20 ±0.03	78.88 ±0.09	76.42 ±0.27	74.03 ±0.07	77.51 ±0.08	86.75 ±0.09	81.38 ±0.09	70.78 ±0.05	73.37 ±0.08	69.94 ±0.17	73.27
	CoDA (Ours)	70.90 ±0.40	71.86 ±0.21	65.99 ±0.23	77.47 ±0.21	73.89 ±0.23	74.46 ±0.15	77.19 ±0.11	72.09 ±0.27	74.31 ±0.14	55.53 ±0.28	76.74 ±0.09	45.78 ±0.16	74.51 ±0.24	78.36 ±0.12	75.22 ±0.10	70.95
LSQ (2-bit)	w/o TTA	34.88 ±0.03	39.95 ±0.19	36.96 ±0.14	47.92 ±0.19	41.50 ±0.12	53.61 ±0.29	51.67 ±0.29	60.97 ±0.14	50.95 ±0.04	54.98 ±0.13	80.14 ±0.21	23.06 ±0.04	65.69 ±0.13	38.23 ±0.08	72.00 ±0.13	50.17
	NORM	58.46 ±0.04	61.17 ±0.46	55.46 ±0.12	67.46 ±0.17	56.32 ±0.15	67.82 ±0.20	69.41 ±0.52	65.25 ±0.35	64.93 ±0.23	67.63 ±0.15	80.76 ±0.17	42.01 ±0.49	71.61 ±0.17	62.34 ±0.39	73.55 ±0.16	64.28
	Tent	65.10 ±0.05	67.51 ±0.15	61.41 ±0.44	73.63 ±0.32	59.06 ±0.12	71.04 ±0.26	74.91 ±0.04	68.14 ±0.47	67.36 ±0.02	67.09 ±0.34	79.83 ±0.15	56.17 ±1.02	70.49 ±0.19	70.12 ±0.05	72.15 ±0.33	68.27
	SAR	62.72 ±0.03	65.24 ±0.31	59.88 ±0.28	71.89 ±0.14	56.89 ±0.43	69.18 ±0.31	72.52 ±0.26	66.02 ±0.32	65.98 ±0.28	63.49 ±0.17	79.10 ±0.08	56.26 ±0.10	68.78 ±0.19	67.34 ±0.23	70.86 ±0.23	66.41
	CoDA (Ours)	70.90 ±0.40	71.86 ±0.21	65.99 ±0.23	77.47 ±0.21	73.89 ±0.23	74.46 ±0.15	77.19 ±0.11	72.09 ±0.27	74.31 ±0.14	55.53 ±0.28	76.74 ±0.09	45.78 ±0.16	74.51 ±0.24	78.36 ±0.12	75.22 ±0.10	70.95
LQ (2-bit)	w/o TTA	45.20 ±0.06	48.97 ±0.22	47.82 ±0.42	52.42 ±0.16	46.04 ±0.06	56.24 ±0.10	55.70 ±0.07	65.97 ±0.03	56.72 ±0.12	59.32 ±0.20	83.53 ±0.11	19.19 ±0.20	68.15 ±0.24	38.16 ±0.14	71.51 ±0.12	54.33
	NORM	63.78 ±0.23	66.26 ±0.37	60.30 ±0.23	69.34 ±0.14	55.66 ±0.18	70.55 ±0.50	71.33 ±0.24	70.78 ±0.03	69.24 ±0.09	71.69 ±0.21	84.35 ±0.24	32.99 ±0.27	71.96 ±0.25	63.61 ±0.23	73.60 ±0.06	66.36
	Tent	69.35 ±0.14	71.58 ±0.02	61.86 ±0.18	80.02 ±0.16	59.27 ±0.52	78.04 ±0.33	79.17 ±0.27	73.53 ±0.19	73.51 ±0.38	75.32 ±0.36	85.08 ±0.21	74.92 ±0.38	72.02 ±0.20	73.30 ±0.17	73.47 ±0.34	73.36
	SAR	69.32 ±0.03	71.60 ±0.04	61.88 ±0.25	80.05 ±0.20	59.30 ±0.40	78.01 ±0.30	79.11 ±0.23	73.55 ±0.19	73.42 ±0.39	75.27 ±0.50	85.10 ±0.34	74.90 ±0.33	72.06 ±0.15	73.30 ±0.19	73.45 ±0.32	73.35
	CoDA (Ours)	72.98 ±0.29	74.26 ±0.12	66.94 ±0.29	83.14 ±0.34	77.69 ±0.15	79.45 ±0.29	81.87 ±0.38	77.01 ±0.36	79.37 ±0.02	67.03 ±0.38	81.68 ±0.19	62.82 ±0.05	78.44 ±0.10	83.32 ±0.26	76.27 ±0.20	76.15

Table 16. Model size and top-1 accuracy (%) comparison on ImageNet-C for each TTA method.

QAT	ResNet18						ResNet50					
	Total num. of bits	w/o TTA	NORM	TENT	SAR	CoDA (Ours)	Total num. of bits	w/o TTA	NORM	TENT	SAR	CoDA (Ours)
FP	374,064,384	22.36	29.13	30.62	33.88	-	27.74	36.20	38.55	41.48	-	-
LSQ (2-bit)	23,380,368	16.25	24.44	27.74	29.47	31.43	51,117,776	19.76	30.44	33.03	34.02	35.22
LQ (2-bit)	23,751,568	18.66	28.35	30.42	30.42	34.27	51,972,304	22.23	32.65	35.03	35.04	38.01
LSQ (4-bit)	46,759,392	19.91	28.50	30.73	31.87	33.50	102,232,096	21.57	31.30	33.70	34.40	36.25
LQ (4-bit)	47,503,136	20.89	28.68	30.07	30.07	34.46	103,944,608	22.96	31.93	33.96	33.95	36.49
LSQ (8-bit)	93,517,440	20.14	29.23	31.25	32.13	34.17	204,460,736	22.58	31.87	34.11	34.87	36.68
LQ (8-bit)	95,006,272	21.11	30.42	31.71	31.70	34.48	207,889,216	13.45	24.08	29.63	29.63	35.02